Green synthesis of graphene-oxide based nanocomposites for efficient removal of methylene blue dye from wastewater

Green Synthesis of Graphene-Oxide Based Nanocomposites for Efficient Removal of Methylene Blue Dye from Wastewater

Kehinde Shola Obayomi [a, c*], Sie Yon Lau [a], Michael K. Danquah [b], Jianhua Zhang [c], Tung Chiong [a], Louise Meunier [d], Stephen R. Gray [c] Mohammad Mahmudur Rahman [e, f]

[a] Department of Chemical Engineering, Curtin University, CDT 250, 98009 Miri, Sarawak, Malaysia

[b] Department of Chemical Engineering, University of Tennessee, Chattanooga 615 McCallie Ave, Chattanooga, TN 37403, United States

[c] Institute for Sustainable Industries and Liveable Cities, Victoria University, Werribee, VIC 3030, Australia

[d] Department of Chemical Engineering, Queen's University, Kingston, K7L 3N6, Canada

[e] Global Centre for Environmental Remediation (GCER), College of Engineering, Science and Environment, The University of Newcastle, Callaghan, NSW 2308, Australia

[f] Department of General Educational Development, Faculty of Science and Information, Technology, Daffodil International University, Ashulia, Savar, Dhaka - 1207, Bangladesh

*Corresponding Author

Tel.: +61477318139

E-mail: obayomikehindeshola@gmail.com

Full postal address: Department of Chemical Engineering, Curtin University Malaysia, CDT 250, 98009 Miri, Sarawak.

Institute for Sustainable Industries and Liveable Cities, Victoria University, Werribee, VIC 3030, Australia

Abstract

Water-soluble dyes are a common problem in wastewater treatment, requiring highly efficient methods for removal. In this study, novel sustainable adsorbents made from graphene-oxide (GO) and other materials, such as eggshell-derived calcium oxide nanoparticles (CaONPs-ES), fish bone calcium oxide nanoparticles (CaONPs-FB), and durian shell activated carbon (DSAC) were synthesized, characterized, and demonstrated for soluble dye removal from wastewater. Fermented maize grain extract (MES) was used as a green cross-linker in the synthesis process. The resulting nanocomposites, GO@CaONPs-ES/DSAC and GO@CaONPs-FB/DSAC, showed promising adsorption capabilities for methylene blue (MB) dye removal from aqueous environments. The prepared nanocomposites (GO@CaONPs-ES/DSAC and GO@CaONPs-FB/DSAC) were characterize using state-of-art instrumental techniques. The BET measurement revealed that the nanocomposites surface areas were enhanced due to the cross-linking phenomenon, improving their adsorption capability towards MB dye treatment. The adsorption data of GO@CaONPs-FB/DSAC and GO@CaONPs-ES/DSAC was well fitted to the Harkins-Jura and Freundlich models, respectively. The maximum sorption capacities of GO@CaONPs-ES/DSAC and GO@CaONPs-FB/DSAC were 1274.5 and 689.7 mg/g, respectively. The MB dye removal mechanism was driven by π-π interaction, hydrogen bonding, electrostatic attraction and physical interactions and the adsorption process of the nanocomposites followed pseudo-second-order kinetics. The adsorptive performance of the nanocomposites was stable, showing ~96.45% and ~85.18% after 10 successive cycles for GO@CaONPs-ES/DSAC and GO@CaONPs-FB/DSAC respectively. Cost evaluation revealed that bulk synthesis of GO@CaONPs-ES/DSAC and GO@CaONPs-FB/DSAC nanocomposites is cost-effective for treating large quantities of MB contaminated water and other potential dyes as well. Finally, the independent and synergetic contributions between pH, adsorbent dosage and temperature on MB removal by GO@CaONPs-ES/DSAC and GO@CaONPs-FB/DSAC were studied and optimized by central composite design (CCD) an aspect of the response surface methodology (RSM).

Keywords: Graphene oxide; Green nanocomposites; Adsorption; Methylene blue dye; Sustainability; Response surface methodology.

1. Introduction

Rapid technological advancements and industrial expansion have led to the contamination of drinking water and the surroundings (Mirzaei et al., 2022). Organic pollutants, predominantly dyes, have been identified as significant sources of water contamination due to their carcinogenicity, toxicity and mutagenicity, with potential posing a risk to aquatic life and human health (Abutaleb et al., 2023). In recent years, the textile, tannery, cosmetic, and food industries have significantly increased the application of dyes, making the treatment of wastewater effluents crucial to aquatic ecosystem and human health, considering the pollutants' , toxicity, non-biodegradability, and persistence in the environment (Zhang et al., 2023a).

Methylene blue (MB) is a universally used cationic organic dye in numerous industries such as textile, chemical indicators, biological stains, pharmaceuticals, food and paper (Said et al., 2023). However, MB dye is an emerging contaminant that can bio-accumulate and persist in the environment, endangering aquatic ecosystems (Mechnou et al., 2022). Exposure to MB dye through water consumption could lead to health challenges such as excessive perspiration, dyspnea, disorientation, cyanosis, eye burn, dermatitis, breathing difficulties, vomiting, tissue necrosis, and nausea (El-Ghobashy et al., 2023). Thus, environmentally sustainable, and highly selective treatment methods to remove pollutants such as MB dye from wastewater before their release into the environment required development.

Over the years, several conventional procedures have been employed for waste water remediation, including flocculation and coagulation, advanced oxidation process, photodegradation, electrochemical, and membrane separation, biodegradation, and ion-exchange (Biswal et al., 2021; Yu et al., 2021; Chouaybi et al., 2022; Gajera et al., 2022; Zhu et al., 2022;). However, these methods have drawbacks, such as the need for specialized equipment, high costs, incomplete dye removal, and the generation of harmful residues (Zhang et al., 2022; Zhu et al., 2023). Adsorption is a promising alternative treatment technique with advantages of high selectivity, economical performance, high removal efficiency, and simplicity of treatment operation (Shi et al., 2022). If the sorbent is accessible and ready for use, adsorption is a promising technique, which is why low-cost adsorbents are gaining rapid attention (Zhu et al., 2023). Recently, several adsorbent substances, such as biochar, nanoparticles, chitosan, clay, and activated carbon, have been employed to treat wastewater dyes (Chen et al., 2022; Thanh et al., 2022; Sellaoui et al., 2023; Obayomi et al., 2023a).

Graphene oxide (GO) synthesis is carried out via the chemical oxidation of graphite material, and it presents an attractive adsorbent as a result of the numerous oxygenated functional groups such as

carbonyl, epoxy, and hydroxyl, which enable it to participate in various bonding interactions that are beneficial for wastewater treatment (Moradi and Panahandeh, 2022). To enhance the capabilities of GO and prevent its particle aggregation, GO can be modified with other materials through decoration and exfoliation, which can significantly improve the sorption performance of the synthesized composites (Obayomi et al., 2023b). Recently, the use of nanocomposite materials as adsorbents has gained considerable attention (Mohamed et al., 2022; Obayomi et al., 2022). The synthesis of nanocomposite materials from low-cost biomaterials and nanoparticles can reduce the cost of adsorbent material preparation and improve adsorption efficiency (Kaveh et al., 2022).

Recent research has also demonstrated that nanoparticles (NPs) made from agricultural waste materials by calcining precursors have excellent pore surface properties that enable effective interparticle interaction of nanoparticles with pollutant species and exhibit a high capacity to remove contaminants from aqueous solutions at a reasonably low cost. (Prajapati and Mondal, 2022; Dedecan et al., 2022). For instance, calcium oxide (CaO) NPs possess unique optical and structural properties and are environmentally friendly, making them suitable for various applications, including catalysis, drug delivery, and environmental remediation (Nazir et al., 2022). Eggshells and fishbones are significant sources of $CaCO_3$, and they could be explored to prepare CaO NPs (Ghaffari et al., 2023).

In addition, activated carbon (AC) offers the best economic advantage of all the carbonaceous allotropes and is widely employed in various industrial applications, primarily as an adsorbent in the treatment of wastewater (Bozaci and Acarali, 2023). The capacity of activated carbon as a sorbent with excellent adsorption affinity is supported by the existence of oxygenated functional groups like hydroxyl and carboxyl on their surface (Neolaka et al., 2023). Furthermore, the use of agricultural waste products, which are abundant in nature, is becoming increasingly important as an alternative to commercial ACs (Devi et al., 2023). Due to its affordability, abundance, cleanliness, and sustainability, durian shell (Durio zibethinus) renewable biomass exhibits significant potential as an AC precursor (Dolas, 2023). Furthermore, the consumption of durians, popularly known as the "king of fruits," is growing because of increased demand, which ensures their continued availability (He et al., 2023). As a result, these durian shells could provide the necessary carbon precursors to increase economic value while addressing the waste problem.

To the best of the authors knowledge, no reported research has been found on the synthesis of CaO NPs from eggshell and fishbone (CaONPs-ES and CaONPs-FB) loaded on GO (GO@CaONPs-ES and GO@CaONPs-FB) and cross-linked with durian shell derived activated carbon (DSAC) using fermented maize extract solution to form a sustainable and eco-friendly nanocomposite (GO@CaONPs-ES/DSAC and GO@CaONPs-FB/DSAC) for the treatment of MB dye. This work aims to develop a green approach for graphene oxide (GO)-based nanocomposites synthesis that

involves a cost-effective and eco-friendly fermented maize extract solution as a cross-linker. Modern analytical methods such as thermogravimetric analysis (TGA), x-ray diffraction (XRD), transmission electron microscope (TEM), fourier transform infra-red spectroscopy (FTIR), x-ray photoelectron spectroscopy (XPS), scanning electron microscopy with energy dispersive spectroscopy (SEM/EDS), Brunauer-Emmett-Teller analysis (BET), and atomic force microscopy (AFM) were employed to investigate the morphology, crystallinity, thermal stability, textural properties, functional groups, chemical state, oxidation state, and surface composition of the GO-based nanocomposites. Additionally, to evaluate the performance of the GO-based nanocomposites and their adsorption characteristics and mechanisms, the treatment of MB dye was investigated in a batch system. The relationship between the operating parameters (pH, adsorbent dosage and temperature) and the MB dye removal onto GO@CaONPs-ES/DSAC and GO@CaONPs-FB/DSAC nanocomposites was established using the central composite design (RSM) under the response surface methodology (RSM) modelling.

2. Materials and Method

2.1 Materials

Analytical grade chemicals such as hydrochloric acid (HCl), graphite, sodium hydroxide (NaOH), potassium hydroxide (KOH), hydrogen peroxide (H_2O_2), methylene blue, sulphuric acid (H_2SO_4), sodium nitrate ($NaNO_3$), and potassium permanganate (KMO_4) were all procured from Merck chemicals, and Sigma-Aldrich, Malaysia. The durian shells and maize grain were procured from e-mart, Miri, Malaysia. The fish bones and eggshells were all obtained from Curtin University Kitchen, Miri Campus, Malaysia.

2.2 Eggshell (ES) and Fish bone (FB) powder preparation

In order to remove dirt, the obtained ES was thoroughly washed several times with distilled water, followed by immersion of the washed ES in 1 % HCl overnight to remove the inner membrane from the shell. After thoroughly washing the inner membrane several time with deionized water, the eggshells were oven dried at 108 ^{o}C for 2 h. The dried eggshells were crushed using mortar and pestle, powdered and sieved to obtain particle size between 125-212 µm. The ES powder was then stored in an airtight plastic bag for use. The FB were boiled for 30 min and washed thoroughly with distilled water to remove unwanted materials. The FB was oven dried at 80 ^{o}C for 12 h, and then powdered using a pestle and mortar. The resultant FB powder was kept in a sealed plastic bag for further use.

2.3 Synthesis of ES and FB derived CaONPs

The Sol-gel method described by Singh et al., (2022) and Kasirajan et al., (2022) was adopted for the preparation of CaONPs from ES and FB powder with slight modifications. The Sol-gel method

is a wet chemical process that involves a three-dimensional network structure formation from an inorganic colloidal suspension in a continuous liquid. The preparation involved the following steps:

30 g each of ES and FB powder were dissolved separately in 500 mL beaker containing 400 mL of 1 M HCl (37 %). The solution was left for 6 hrs until there was effervescence cessation, which indicated the formation of calcium chloride ($CaCl_2$) according to chemical equations (1).

$$ES/CaCO_3\ (g) + 2HCl\ (aq) \rightarrow CaCl_2\ (aq) + H_2O\ (l) + CO_2\ (g) \quad (1a)$$

$$FB/CaCO_3\ (g) + 2HCl\ (aq) \rightarrow CaCl_2\ (aq) + H_2O\ (l) + CO_2\ (g) \quad (1b)$$

Thereafter, 300 mL of 98 % NaOH (1 M) was introduced to each beaker dropwise using a burette, resulting in the synthesis of calcium hydroxide ($Ca(OH_2)$ precipitate according to equation (2). The $Ca(OH)_2$ precipitate was centrifuged for 20 min at 3000 rpm. The resultant $Ca(OH)_2$-derived ES ($Ca(OH)_2$ -ES) and FB ($Ca(OH)_2$ -FB) powder was washed with ultra-pure water and dried in an oven for at 80 ^oC for 3 h.

$$CaCl_2\ (aq) + 2Na(OH)_2\ (aq) \rightarrow Ca(OH)_2\ (s) + 2NaCl\ (aq) \quad (2)$$

Finally, the dried $Ca(OH)_2$ derived from ESP was calcined in muffle furnace at 900 ^oC while the $Ca(OH)_2$ derived from FB powder was calcined in a furnace at 1000 ^oC for 1 h to obtain a white colour calcium oxide nanoparticles. See equation (3). The resultant products were stored in plastic bags and labelled CaONPs-ES and CaONPs-FB, respectively.

$$Ca(OH)_2\ (s) \xrightarrow{heat} CaO\ (s) + H_2O\ (l) \quad (3)$$

2.4 Development of durian shell-derived activated carbon (DSAC)

The durian shells (*Durio zibethinus)* were chopped and reduced to smaller sizes. Dirt and unwanted materials were removed by washing with water (distilled). The shells were left to sun-dry for 10 h, then transferred to an oven for drying at 110 ^oC for 18 h. 100 g of the dried durian shell was weighed into crucibles and transferred into a muffle furnace set at 550 ^oC. Thereafter, at a 10 mL/min flow rate, nitrogen gas (N_2) was introduced to the tubular furnace at a 15 ^oC/min heating rate for 20 min. The furnace was allowed to heat until the temperature under the same nitogen flow attained 550 ^oC. The furnace temperature was maintained for 60 min. After completion of the carbonization process, the biochar was removed and left at room temperature to cool. The cooled biochar was then subjected to activation by impregnation. The biochar was activated chemically by immersing in 1000 mL beaker containing 500 mL of 2 M KOH and incubated overnight at room temperature. After the activation process was complete, HCL (1 M) was used to wash the mixture followed by distilled water until a neutral pH (pH 6.7-7) was achieved. The activated sample was then dried

steadily in an oven at 80 ^{o}C for 24 h. The resultant durian shell-activated carbon (DSAC) was stored in a plastic bag until needed.

2.5 Synthesis of graphene oxide (GO)

The Hummers' method as described by Sarkar et al., (2022) was employed for the preparation of GO with slight modifications. Briefly, 5 g of powdered graphite (99 % purity), sodium nitrate (2.5 g) and 90 mL sulphuric acid (98 %) were placed into a beaker (250 mL) inside an ice bath under continuous stirring for 2 h at 10 ^{o}C to ensure homogeneous mixture. 30 g of potassium manganate was added slowly at regular time intervals to the mixture in the ice bath to keep the reaction temperature at below 10 ^{o}C. The stirring of the mixture continued for 2 h in an ice bath. The ice bath was then taken away, and the mixture was stirred overnight at 35 ^{o}C. The mixture gradually thickened, resulting in a brown colour change. Following the reaction, 150 mL of water was added dropwise to the brown paste which triggered an exothermic reaction that produced heat, thereby raising the reaction temperature of the mixture to about 98 ^{o}C. The beaker was left to cool at room temperature, thereafter, 30 % hydrogen peroxide (50 mL) was introduced in drops to the mixture until a golden yellow colouration was established. The mixture was centrifuged, washed several times with 5 % HCl and water (deionized). After washing, the mixture was filtered, and oven dried at 60 ^{o}C overnight. Finally, the dried form of as-prepared GO was kept in a sealed container until further use.

2.6 Synthesis of fermented maize extract solution (MES)

The fermented maize extract solution (MES) was synthesized using the technique described by Ndagijimana et al., (2022) with slight modifications. A known quantity (30 g) of maize grains was sorted and washed to remove dirt and unwanted materials. The washed grains were steeped in a 1000 mL beaker containing ultra-pure water (500 mL) and left for 72 h to ferment. Next, the fermented grains were drained and wet-milled into a slurry. The slurry was sieved through a muslin cloth to obtain the MES. The MES was left at room temperature for another 48 h to allow for further fermentation. Finally, the MES was employed as a green cross-linker.

2.7 Fabrication of GO incorporated-CaONPs cross-linked DSAC (GO@CaONPs/DSAC)

The hydrothermal treatment method reported by Yasin et al., (2021) with slight modifications was employed. 4 g each of CaONPs-ES and CaONPs-FB was dissolved several 250 mL beakers containing ultra-pure water (100 mL) and continuously stirred at room temperature on a magnetic stirrer. Thereafter, 2 g of GO was introduced to the mixtures under continuous stirring, and the resultant mixtures were stirred vigorously for 3 h followed by ultrasonication for another 2 h. After ultrasonication, the mixtures were stirred for another 2 h to ensure homogeneity. The mixtures were treated hydrothermally in a Teflon-lined autoclave (100 mL) at 120 ^{o}C for 18 h, cooled at room temperature, washed several times with ultra-pure water, and oven dried at for 24 h at 70 ^{o}C. Finally,

the dried samples were calcined for 2 h at 400 ^{o}C in a muffle furnace in order to get rid of impurities, allowed to cool to room temperature and labelled as GO@CaONPs-ES and GO@CaONPs-FB. Furthermore, 3g each of GO@CaONPs-ES and GO@CaONPs-FB were transferred separately into several 250 mL beakers with 100 mL of ultra-pure water. The mixtures were stirred on a magnetic stirrer for 30 min at 70 ^{o}C. 5 g of DSAC was introduced into the mixtures under continuous stirring for another 20 min with subsequent addition of 3 mL MES. The mixtures were stirred for additional 10 min and cool to room temperature. The resultant black precipitate was washed, oven dried for 12 h at 105 ^{o}C and thermally treated for 1 h at 550 ^{o}C. Finally, the as-prepared GO-based nanocomposites (GO@CaONPs-ES/DSAC and GO@CaONPs-FB/DSAC) were stored in airtight plastics bags until further use.

2.8 GO-based nanocomposites characterization

The fabricated GO-based nanocomposites materials before and after adsorption studies were characterized to investigate the structural, textural, crystallinity, surface chemistry, thermal stability, and elemental composition as well as the chemical and atomic electronic state within the adsorbent materials. The morphological structures and elemental components of the fabricated materials were assessed with a scanning electron microscope (SEM) fitted with an energy dispersive x-ray analyzer (SEM-EDS, QUANTA 450 FEG D9844, FEI, Australia, and Xplore EDS detector with AztecLiveLiteL software, Oxford Instruments). The material's surface chemistries were investigated via Fourier transform infrared spectroscopy (FTIR, Agilent Cary 660). The materials surface area examinations were performed using a Brunauer Emmett and Teller analyzer (BET, TriStar II 3020, Micromeritics) at 77.36 K. The surface potential of the nanocomposites was analyzed using a Zeta potentiometer (NanoPlus-3 HD, Zeta Potential and Nano Particle Analyzer, Micromeritics). Powdered X-ray diffraction (PXRD, AXS D8 advance, Bruker, Billerica, MA, USA) with Cu Kα radiation (Kα = 1.541 Å) was utilized to provide insights on the crystallographic, structural and physical composition and properties of the prepared materials. The thermal stability of the materials was investigated under N_2 atmosphere with a thermogravimetric analyzer (TGA, Pyris 1 model, PerkinElmer, Waltham, MA, USA) with the 10 ◦C min−1) heating rate at a range of temperature from 5–1000 ^{o}C. The atomic electronic state, chemical structure, and elemental composition of the synthesized materials were determined using the X-ray Photoelectron Spectroscopy (XPS, Mg Ka (1253.6 eV), Kratos Axis Ultra DLD, UK). The surface topography was performed using the Atomic force microscopy (Cypher AFM, Oxford Instruments, UK) and Size distribution and shape were also determined using a high-resolution transmission electron microscope (HRTEM, JEM-2100F, Japan).

2.9 Equilibrium batch adsorption studies

Standard stock solution (1000 mg/L) of the MB dye was made by dissolving MB (500 mg) in 500 mL of deionized water. In order to avoid photodegredation, the homogeneous mixture was kept in a dark glass bottle. Serial dilution was used to create MB dye working concentrations between 10 and 50 mg/L from the stock solution. Batch equilibrium adsorption studies were investigated at various temperatures of 298, 308, and 318 K using several Erlenmeyer flasks (250 mL) with varying concentrations of MB (10-50 mg/L). In each flask, fifty (50) mg of GO@CaONPs-ES/DSAC or GO@CaONPs-FB/DSAC) was added while retaining the initial pH value of the MB solution. To improve the surface interactions between the adsorbate and prepared adsorbents, the flasks were stirred and put in an isothermal shaker for 180 minutes at a controlled temperature with a constant shaker speed of 160 rpm. Prior to equilibrium attainment, MB was sampled periodically and analysed using a UV-VIS spectrophotometer (Shimadzu UV-1601 spectrophotometer, Japan) at 664 nm. The percentage removal of MB at different time intervals and the quantity of adsorbate adsorbed at equilibrium and at time (t) were evaluated using equations 4 -6:

$$\%\ MB\ removal = \left(\frac{C_f - C_o}{C_o}\right) \times 100 \quad (4)$$

$$q_e = \frac{(C_0 - C_e)\,V}{W} \quad (5)$$

$$q_t = \frac{(C_0 - C_t)\,V}{W} \quad (6)$$

Where C_f and C_o are the final and initial concentration of MB dye in mg/g; C_t and C_e represents the equilibrium concentration at time, t (mg/g) and equilibrium concentration: V stands for the dye solutions volume (L); and W represents the adsorbent weight of adsorbent (g).

The pH of MB dye solutions in each flask was set from 2 to 11 by addition of HNO_3 (0.1 M) and NaOH (0.1 M). The mixtures were continuously agitated at a temperature of 318 K for 60 minutes at 160 rpm using an isotherm shaker. The impact of adsorbent dosage on MB removal was determined via a batch adsorption system. The dosage of GO-based nanocomposites was varied from 10 to 60 g/L, while the MB dye concentration was left constant at 50 mg/L. The agitation time was fixed at 60 min, the temperature at 318 K, and the shaker speed at 160 rpm. To ascertain the pH point of zero charge (PZC), a set Erlenmeyer flasks (100 mL) were used. Firstly, 50 mL of NaOH (0.1 M) was added to each flask, and then 50 mg of the nanocomposite adsorbents were added. NaCl solution pH was adjusted between 2 and 11 by introducing NaOH (1 M) and HCl to each flask. The flasks were positioned in an incubator shaker for 4 hours at 160 rpm to allow the NaCl solution and the adsorbents to attain equilibrium. Afterward, the Zeta potential was used to determine the solutions pH.

2.10 MB removal optimization

In this study, a segment of the response surface methodology (RSM), central composites design (CCD) amongst other designs, was used to analysis the individual and synergetic effect of selected parameters (temperature, adsorbent dosage, and pH) on MB removal to optimize the performance. The three operations which characterized the CCD are: 2n axial runs (6 points), 2n factorial runs (8 points), and six center runs (6 point), resulting in a total experimental run of 20. The optimal predictor quadratic equation model given in Equation 1 was used to correlate the parameters and the responses

$$y = \beta_o + \sum_{i=1}^{k} \beta_i X_i + \sum_{i=1}^{k} \beta_{ii} X_i^2 + \sum_{i<j} \beta_{ij} X_i X_j \quad (7)$$

where y is the response predicted, β_o is the coefficient constant, $\beta_i, \beta_{ii}, \beta_{ij}$, denotes linear, quadratic and interaction coefficients, and Xi, Xj is the independent parameters. The regression analysis was performed by Design Expert (version 11.0) statistical software to fit the equations for the responses and to assess the statistical significance of the equations derived with the help of the experimental data. The responses variability was evaluated using the Fishers value (F-value), probability value (P-value, with confidence level of 95 %), and coefficient of determination (R^2). The independent parameters range values and their coded levels are shown in Table 1.

Table 1. Independent parameters range values and coded levels for the CCD

Parameter	Code	Unit	Range and coded levels		
			-1	0	1
Temperature	A	K	298	308	318
Adsorbent dosage	B	g/L	0.1	0.3	0.5
pH	C	-	6	8	10

3. Result and discussions

3.1 Characterization of the nanocomposites

3.1.1 XRD analysis

The XRD patterns for the GO@CaONPs-ES/DSAC and GO@CaONPs-FB/DSAC composites are presented in Fig. 1(a-b), respectively. The incorporation of DSAC and CaONPs into the GO matrix resulted in the formation of new peaks, while some peaks remained unchanged, and others shifted to the left or right. The peaks at 29.43º, 34.2º, 47.1º, 54.4º, 62.7º, and 64.3º (JCPDF # 77-2376) observed in Fig. 1(a) can be attributed to CaO derived eggshell. Additionally, the GO peak at 42.8º assigned to (100) was detected. The broad peak of carbon at 24.2º (002) shifted to 25.5º. The disappearance of the GO diffraction peak at 11.5° in the XRD pattern of the GO@CaONPs-ES/DSAC composite (Fig. 1(a)) may be attributed to a small amount of GO added to the mixture or favorable dispersion of GO nanoparticles and interfacial interactions within the matrix (Rostamian et al., 2022). The diffraction peaks of DSAC, CaO, and GO observed in Fig. 1(a) indicate the

successful incorporation of DSAC and CaO into the GO matrix, forming the GO@CaONPs-ES/DSAC composite. The XRD pattern of the GO@CaONPs-FB/DSAC composite (Fig. 1(b)) also revealed the presence of carbon, CaO, and GO at their respective peak positions with slight shifts but with lower intensities when compared. The shift in the GO peak from 11.2º to 17.1º suggests that the GO layer sheets may have been exfoliated, and the DSAC and CaONPs may have been introduced in these layers (Bayantong et al., 2021). The shift in the DSAC peak from 24.2º to 26.02º and 29.3º to 27.9º, respectively, can be attributed to the incorporation of DSAC into the GO matrix. The remaining peaks at 31.5º, 34.6º, 39.4º, 46.5º, 49.5º, 53.5º, and 64.31º (CaO XRD standard pattern) resemble the CaO (derived fish bone) phase. It is evident that the peaks in the GO@CaONPs-FB/DSAC nanocomposite are noticeable, indicating the successful incorporation of CaONPs and DSAC into the GO matrix (Fig. 1(b)). The size of the prepared GO@CaONPs-ES/DSAC, and GO@CaONPs-FB/DSAC was determined using the Debye-Scherrer equation, which is given by:

$$D = \frac{0.94\lambda}{\beta \cos\theta} \quad (8)$$

Where D stands for the crystalline size of the nanoparticles, $\boldsymbol{\lambda}$ represents the wavelength, $\boldsymbol{\beta}$ represents the average full width half maximum calculation and θ is the diffraction angle (Bragg angle) (Singh et al., 2022). The average crystallite size of the GO@CaONPS-ES/DSAC, and GO@CaONPS-FB/DSAC calculated were 13.34 and 15.63 nm, respectively.

3.1.2 FT-IR analysis

As shown in Fig. 1, the FTIR patterns of the GO materials revealed the presence of a broad absorption peak at 3468 cm^{-1} corresponding to O-H stretching vibration of the hydroxyl group due to adsorbed water molecule (Sajjad et al., 2022). The peak at 1751 cm^{-1} may be assigned to the C=O (-COOH) stretching vibration of the carboxyl group (Rostamian et al., 2022). The emergence of absorption bands at 1630 and 1570 cm^{-1} could be due to C = C stretching vibration, while other peaks in the GO spectrum located at 1416 and 1149 cm^{-1} correspond to C-OH and C-O of the epoxide group (Babakir et al., 2022). The IR spectrum of DSAC displays a broad peak at 3468 cm^{-1} corresponding to the O-H stretching vibration of the hydroxyl groups found in lignin, cellulose and hemicellulose. The absorption peaks at 2904 and 1630 cm^{-1} could be attributed to the aliphatic C-H group and C=O stretching vibration of the carboxyl group and hemicellulose, respectively (Jawad et al., 2022). The absorption bands at 1570 and 1416 cm^{-1} revealed the presence of axial deformation of C=C aromatic lignin and C-OH stretching (Joshiba et al., 2022). The IR spectra of CaONPs-ES presented in Fig. 1(c), displayed sharp and broad peaks at 3641 and 3468 cm^{-1} corresponding to O-H group due to absorbed water molecule on the CaONPs surface (Ayyaz et al., 2022). The adsorption bands at 2356, 1797, 1643, and 1416 cm^{-1} which are also present in

the spectra of ES could be assigned to the existence of C=C, C=O, and C-O stretching vibrations (Kumar et al., 2022). The band at 1083 cm^{-1} relates to C-O stretching. The peak at 868 cm^{-1} is attributed to the Ca-O stretching vibration, confirming the successful synthesis of CaONPs (Moghaddas et al., 2022). The IR spectra of CaONPs-FB in Fig. 1(d) shows the presence of absorption bands at 3641 and 3468 cm^{-1} corresponding to the stretching vibration of O-H group. The band at 2360 cm^{-1} may be due to the O=C=O stretching of the carbon dioxide group (Agalya et al., 2022). The peak at 1662 cm^{-1} is associated with the C-H bending vibration. The band located at 1068 cm^{-1} is assigned to C-N stretching, demonstrating the presence of non-degenerate symmetric stretching of the phosphate groups and amine groups. The peak located at 721 cm^{-1} is attributed to Ca-O stretching, confirming the presence of CaONPs. The absorption band at 567 cm^{-1} shows the P-O degenerated bending mode (Jyotsna and Vijayakumar, 2020). The successful formation of GO@CaONPs-ES/DSAC composite was assessed and confirmed by comparing the IR spectra of GO, DSAC, CaONPs-ES with the synthesized GO@CaONPs-ES/DSAC spectra as shown in Fig. 1(c). The GO@CaONPs-ES/DSAC composite spectrum shows that some peaks of both GO, DSAC and CaONPs-ES are present while others disappeared, confirming that DSAC and CaONPs-ES were successfully deposited on the surface of GO (Babakir et al., 2022). The absorption peaks at 3641 and 3468 (O-H), 1643 (C=O), 1416 (O-H deformation of the C–OH group) and 1149 (epoxy C-O), and 868 cm^{-1} (Ca-O) of individual functional groups of GO, CaONPs-ES, and DSAC were significantly present in the nanocomposite due to strong interaction, indicating the presence of CaONPs-ES and DSAC on the GO active surface (Rostamian et al., 2022). The formation of GO@CaONPs-FB/DSAC nanocomposite was successfully confirmed from the FT-IR spectra as presented in Fig. 1(d). The successful synthesis of GO@CaONPs-FB/DSAC was indicated by the assignment of several absorption peaks at 3468, 2360, 1630, 1068, 613, and 567 cm^{-1} corresponding to O-H vibration stretching, aliphatic C-H group, C-N stretching (presence of amine groups and non-degenerate symmetric stretching of the phosphate groups), Ca-O, and asymmetric stretching vibration of O-P-O (Yadav et al., 2022). The collection of peaks corresponding to several functional groups in the GO@CaONPs-FB/DSAC nanocomposite confirms the successful attachment of CaONPs-FB and DSAC on the GO surface (Mahmoud et al., 2022).

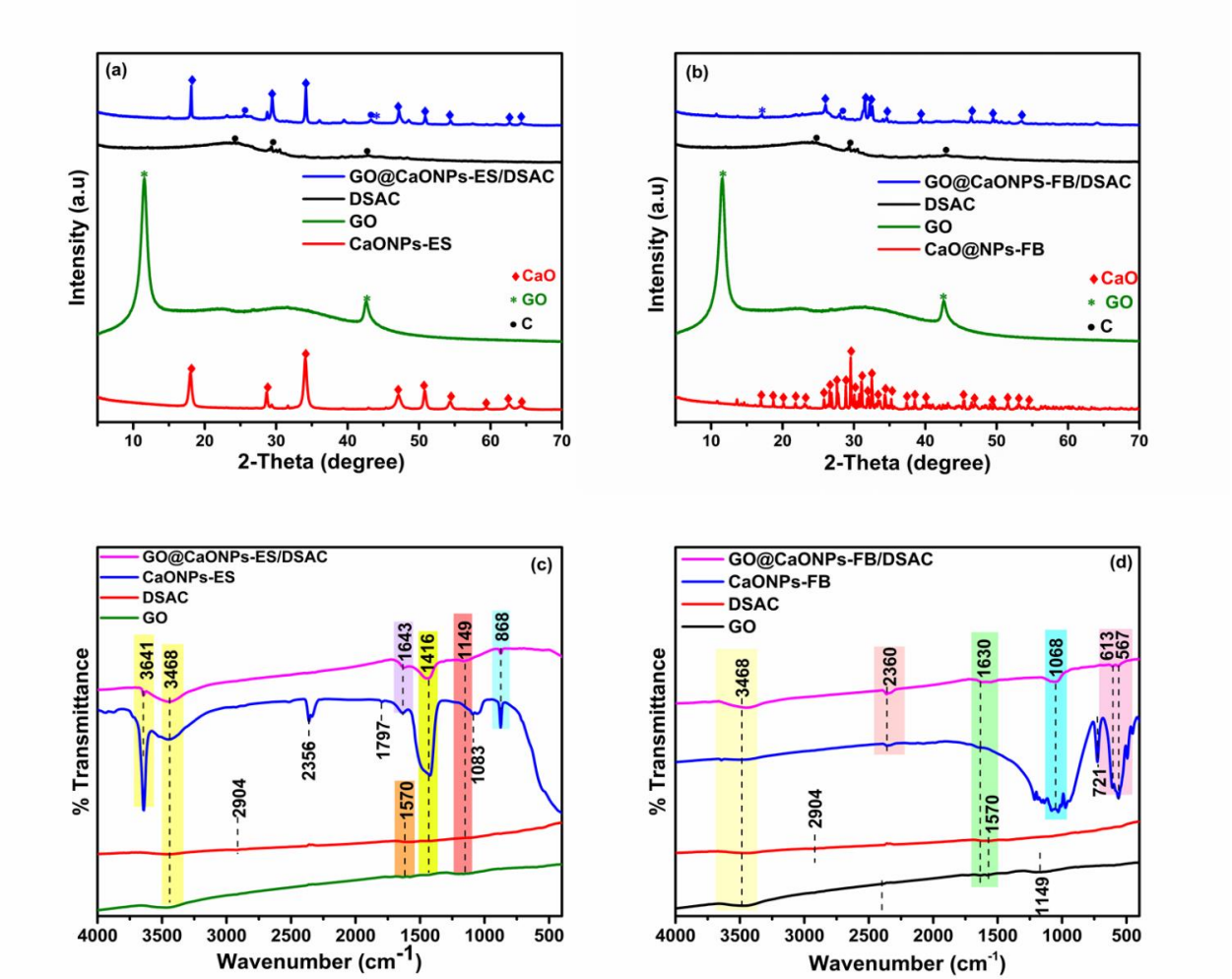

Fig. 1. XRD (a-b) and FT-IR (c-d) analyses of GO@CaONPs-ES/DSAC and GO@CaONPs-FB/DSAC composites

3.1.3 Thermogravimetric (TGA) analysis

The thermal stability of the fabricated composite materials was examined by means of thermogravimetric (TGA) and derivative thermogravimetric (DTG) analyses, as presented in Figure S1(a-f). The TGA curve for DSAC, shown in Figure S1(a), indicated a rapid decrease in weight starting at around 905°C. The DTG curve revealed the highest rate of weight loss at approximately 913°C, which could be attributed to the breakdown of cellulose and hemicellulose (Zhang et al., 2023a). The weight of the DSAC remained constant after approximately 930°C, accounting for nearly 15% of the initial weight, suggesting that the remaining materials from the carbonization process were lignin and ash (Wang et al., 2022). The TGA and DTG curves for GO exhibited four distinct weight loss stages, as shown in Figure S1(b). The initial weight loss of 21.2% between temperatures of 25-134°C could be attributed to the pyrolysis of oxygenated functional materials and the evaporation of adsorbed water (Jia et al., 2023). The weight loss of 9.9% observed between 134-198°C was likely due to labile oxygen-containing functional groups such as hydroxyl, epoxy, and, which are in significant concentrations on the GO surface. The weight loss of about 15.1% observed between the temperature range of 196-296°C may be attributed to the complete oxidation

of the graphite material (Nascimento et al., 2022). The decrease in weight loss of 5.6% observed between 296-394°C can be attributed to carboxylic decomposition, resulting in the release of CO_2 gas. The GO material was seen to be thermally stable between 394-611°C. The peaks observed at 78, 142, 269, and 612°C, as revealed by the DTG curve, indicate the various stages of thermal decomposition of GO resulting from the oxygen-containing functional groups. The TGA and DTG curves for CaO nanoparticles derived from fish bone (CaONPs-FB) and eggshell (CaONPs-ES) were presented in Figures S1(c-d). The CaONPs-FB depicted in Figure S1(c) showed a weight loss of 0.81% between 53-898°C, attributed to the evaporation of adsorbed water. The second weight loss of 0.53% between 898-910°C could be ascribed to the decomposition of $Ca(OH)_2$ into CaO. Finally, the weight loss of 0.06% observed between 910-1000°C may be due to the decomposition of unreacted $CaCO_3$ into CaO and CO_2. The TGA and DTG curves for CaONPs-ES, as shown in Figure S1(d), demonstrated a weight loss of 3.22% between the temperature range of 45–389°C, attributed to the vaporization of adsorbed water (Tan et al., 2022). The weight loss of 21.4% within the temperature range 389-447°C could be attributed to the $Ca(OH)_2$ decomposition into CaO (Jalu et al., 2021). The CaONPs-ES was found to be thermally stable with no significant weight loss recorded above 447°C, and the total weight loss after this temperature was 24.6%. The DTG curve of CaONPs-ES showed a maximum temperature peak at 435°C. Further heating to 900°C may have triggered calcination, leading to desorption of CO_2 and the formation of CaO. The TGA and DTG profiles illustrating weight loss as a function of reaction temperature for the GO@CaONPs-FB/DSAC and GO@CaONPs-ES/DSAC nanocomposites are presented in Figure S1(e-f). The maximum weight loss demonstrates a bias towards higher temperatures, which could be attributed to the limitations on mass and heat transfer within the sample, leading to an increased temperature difference between the sample and the furnace. Additionally, the DTG curve reveals that maximum weight loss decreases as the heating rate rises due to mass transfer likely occurring during heat conduction from the exterior to the interior surface at higher heating rates (Hussain et al., 2019). The TGA and DTG profiles of the GO@CaONPs-ES/DSAC nanocomposite is presented in Figure S1(e). The weight loss of 3.8% between 25-447 ^oC may be attributed to moisture removal and de-volatilization of volatile organic matter. The weight loss of 14.1% between 447-745 ^oC could be due to the graphitization of carbonaceous materials. Finally, the maximum weight loss of 17.9 % occurred between 745-1000 ^oC, which may be attributed to the incorporation of CaO-ES and DSAC on the surface of GO (Farivar et al., 2021). The TGA and DTG profiles of GO@CaONPs-FB/DSAC nanocomposite in Figure S1(f), indicates that moisture loss and de-volatilization occur at temperatures ranging from 25-110 ^oC, after which weight loss increases rapidly. The weight loss of 26.3% observed between 109-1000 ^oC could be attributed to the incorporation of CaO and DSAC on the surface of GO. The DTG peak with the greatest visual impact and prominence may be due to devolatilization, in which volatile substances are released from the sample. However, during this

process, gases and light chemical compounds are released due to breakdown events that weaken and break chemical bonds, releasing a significant amount of heat and producing highly exothermic effects (Shagali et al., 2023).

3.1.4 SEM/EDX and TEM characterization

The surface micrographs and elemental contents of MES, GO@CaONPs-ES/DSAC, and GO@CaONPs-FB/DSAC are depicted in 2(a-f). The MES image presented in Fig. 2(a) revealed a joint layer of inter-wooven fibres that could support flexibility and mechanical strength. making it a good choice to be employ as a cross-linker. The SEM images of GO@CaONPs-ES/DSAC, and GO@CaONPs-FB/DSAC morphologies displayed in Fig. 2(a-b), revealed a rough, uneven surfaces with large pores and cavities, thereby making them a good adsorbent for pollutant removal (Jawad et al., 2022). The surface of the composites was observed to be covered with small white particles, which could be attributed to the decoration of CaONPs on the GO surface (Han et al., 2023). The particles are more obvious on the surface of GO@CaONPs-FB/DSAC (Fig. 2(c)). Furthermore, the EDX analysis was investigated in this study to investigate the elemental compositions and verified the role of MES during the cross-linking process of GO@CaONPs-ES/DSAC, and GO@CaONPs-FB/DSAC formation as presented in Fig. 2(d-f). The EDX analysis of MES presented in Fig. 2(d), confirmed the presence of carbon (61.4%), oxygen (36.5%), sulphur (1.2%), phosphorous (0.6%), magnesium (0.2%), and potassium (0.1%). The weight percentage of Calcium in the GO@CaONPs-ES/DSAC, and GO@CaONPs-FB/DSAC samples were 10.7 and 11.7% respectively, which verified the presence of CaONPs in the developed composites. displayed in Fig. 2(e-f), confirmed the presence and uniform distribution of CaONPs in the composites. The oxygen content of (65.0 and 60.3%) and carbon (23.7 and 26.6%) contents in the GO@CaONPs-ES/DSAC, and GO@CaONPs-FB/DSAC were derived from GO and DSAC during the cross-linking process. The high oxygen content in the composites could be attributed to the introduction of more oxygen-contained groups during the synthesis process, suggesting the successful formation of GO@CaONPs-ES/DSAC, and GO@CaONPs-FB/DSAC. In addition, the presence of sulphur, potassium, magnesium, phosphorous in GO@CaONPs-ES/DSAC, and GO@CaONPs-FB/DSAC composites were due to the introduction of MES responsible for the formation of intermolecular cross-linkage with functional groups such as carbonyl, carboxyl, epoxide, and hydroxyl groups present I GO, DSAC and CaONPs during the cross-linking process (Ndagijimana et al., 2022). This phenomenon further reconfirmed the successful loading of CaONPs on GO surface cross-linked with DSAC. The TEM measurement of GO@CaONPs-ES/DSAC, and GO@CaONPs-FB/DSAC at different magnifications were presented in Fig. 2(g-J). revealed that GO@CaONPs-ES/DSAC, and GO@CaONPs-FB/DSAC particles display a wurtzite shape which are polydispersed (Fig. 2(g

& i)) with average particle sizes ranging from 11 to 21 nm and 4-14 nm, respectively (see Fig. 2(h & j)) (Raza et al., 2022).

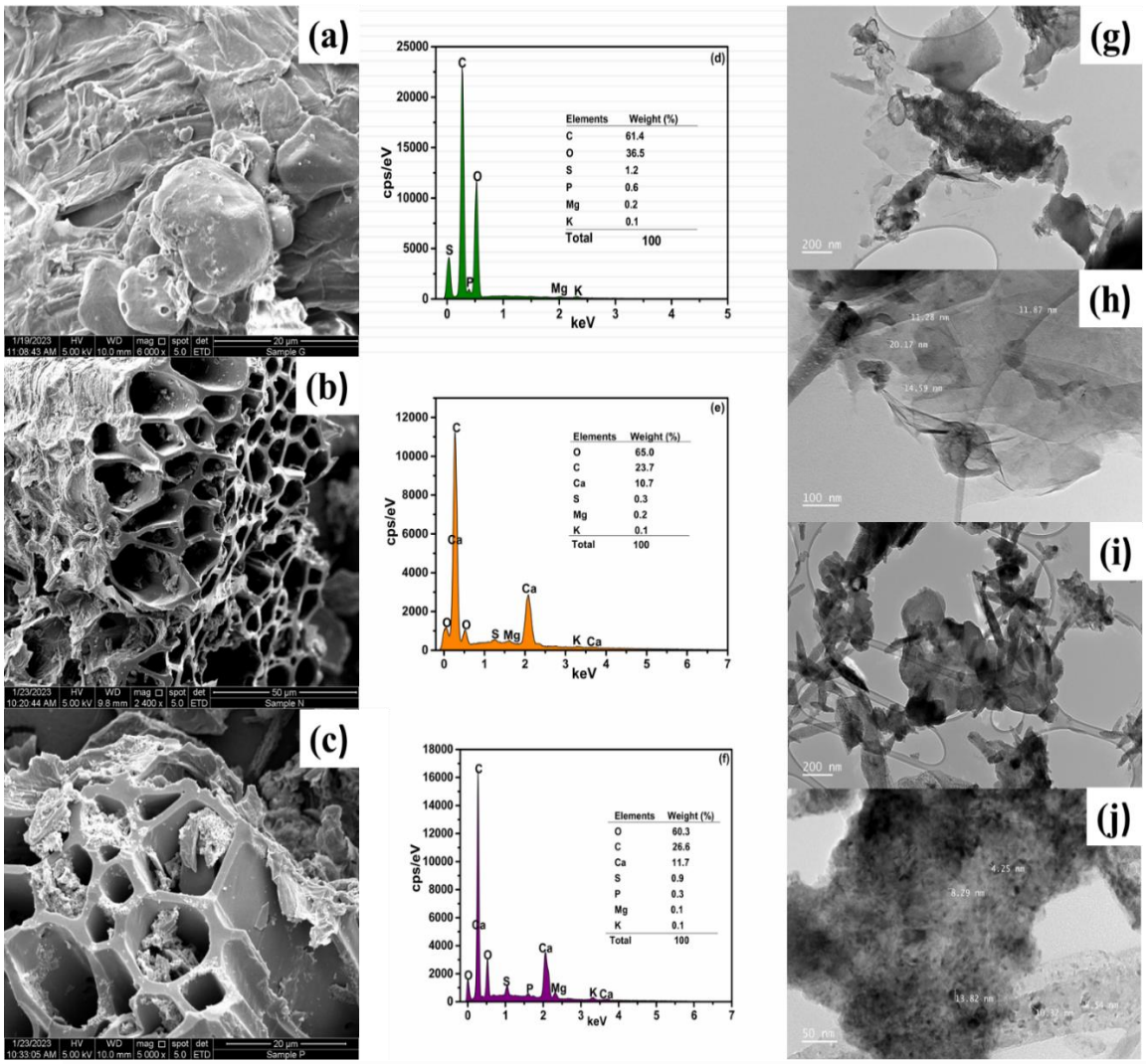

Fig. 2. SEM micrographs and elemental contents of MES, GO@CaONPs-ES/DSAC, and GO@CaONPs-FB/DSAC (a-f), and TEM images of GO@CaONPs-ES/DSAC, and GO@CaONPs-FB/DSAC at different magnifications (g-j)

3.1.5 AFM analysis

The AFM analysis was conducted under ambient conditions using tapping mode probes with constant amplitude. Scanning was carried out at multiple positions of each sample and representative images are displayed here. Roughness parameters were estimated using a nasoscope image processing software. The roughness and topography of the developed nanocomposites were examined with AFM analysis as shown in Fig.3(a-b). The surface roughness was quantified using the average roughness (R_a), maximum surface roughness (R_m), root mean square (Rq), and bearing analysis as presented in Table 2. The average roughness (R_a) is the absolute surface average roughness relative to the base length while the average roughness (R_a) measures the surface deviations from the adsorbents mean plane (Kayanja et al, 2023).

Table 2. Quantitative parameters from AFM analysis

Adsorbent	Roughness average (R_a) (nm)	Root mean square (R_q) (nm)	R_q-R_a (nm)	Maximum roughness (R_m) (nm)	Bearing area (μm^2)	Bearing area (%)
GO@CaONPS-ES/DSAC	103.7	129.6	25.9	530.8	27.7	10.7
GO@CaONPS-FB/DSAC	130.6	158.4	27.8	531.4	30.6	22.4

Usually, R_q and R_a are similar, if there is no large deviation from the mean surface level. The higher value of R_q-R_a for GO@CaONPs-ES/DSAC (25.9 nm) and GO@CaONPs-FB/DSAC (27.8 nm), confirms the presence of filler particles on the nanocomposite's surfaces (George et al., 2016). However, one of the major shortcomings of roughness analysis is that it does not display the lateral spacing's of the surface feature. The bearing analysis estimates the particle distribution as well as the dimensions and filler parts in the matrix. The bearing area of GO@CaONPs-ES/DSAC and GO@CaONPs-FB/DSAC were 10.7 % (27.7 μm^2) and 22.4 % (30.6 μm^2), respectively. The high surface roughness of both composites as depicted in Table 2, could be attributed to the surface porosity and pore diameter owing to the anchoring and cross-linking ability of CaONPs and DSAC on the GO surface, suggesting a favourable surface for MB dye adsorption (Zhang et al., 2023b).

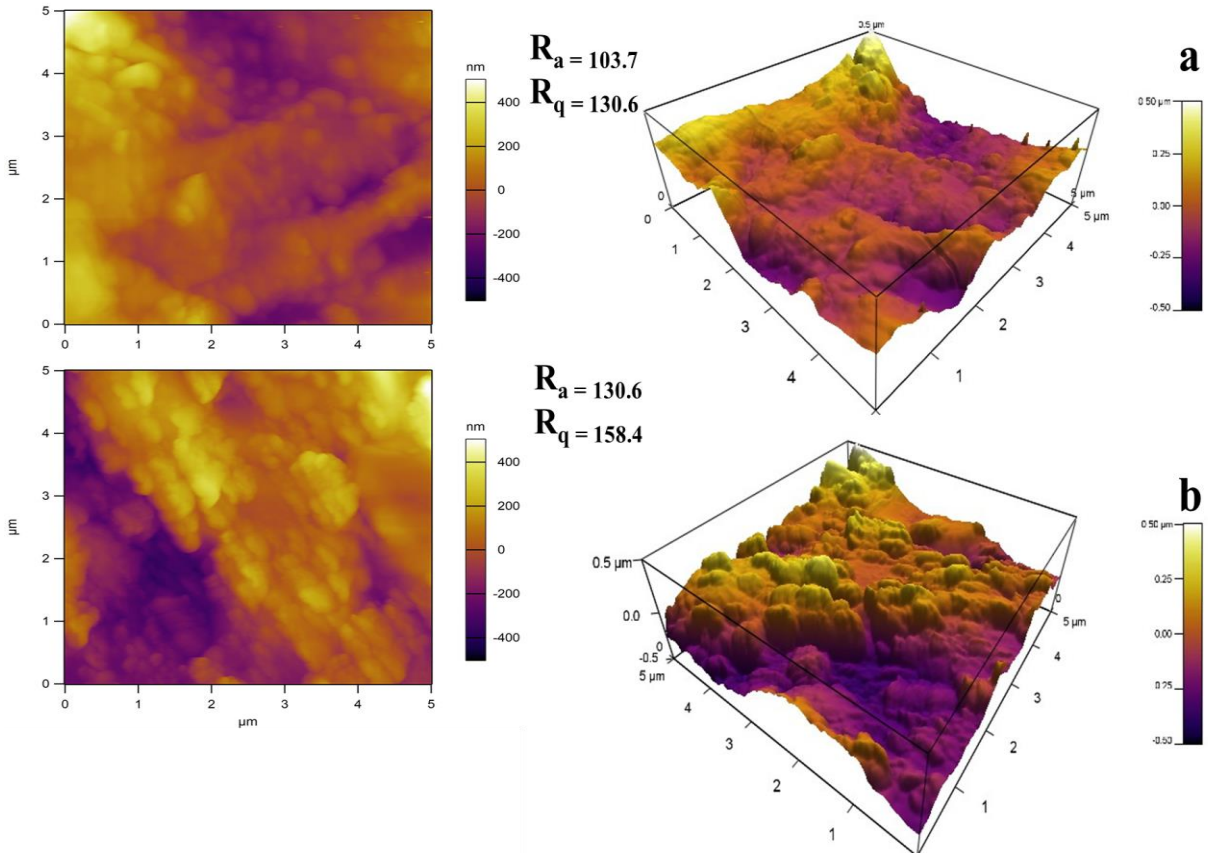

Fig. 3. AFM analysis of (a) GO@CaONPS-ES/DSAC, and (b) GO@CaONPS-FB/DSAC nanocomposite

3.1.6 BET characterization

The nitrogen adsorption-desorption isotherm was employed to examine the BET specific surface area, pore diameter, and volume of the synthesized materials, including GO, DSAC, CaONPs-ES, CaONPs-FB, GO@CaONPs-ES/DSAC, and GO@CaONPs-FB/DSAC. The plots presented in Fig. S2(a-f) indicated that all synthesized materials exhibited a type IV isotherm behavior, with a prominent hysteresis loop at high relative pressure. According to the classification system established by the International Union of Pure and Applied Chemistry (IUPAC), the majority of pores in the materials were found to be mesoporous in nature (2-50 nm). The BET surface area, pore volume, and average diameter for DSAC, GO, CaONPs-ES, and CaONPs-FB were found to be 698.23, 82.41, 61.88, and 47.43 m^2/g; 0.165, 0.0303, 0.00311, and 0.00551 cm^3/g; and 5.88, 3.48, 4.90, and 4.55 nm, respectively (see Table 3). The high surface area of DSAC could be attributed to the intercalation of potassium metal resulting from the intermediate reaction between carbon and KOH due to the hydrolysis of potassium metal (Obayomi et al., 2023c). The GO@CaONPs-ES/DSAC and GO@CaONPs-FB/DSAC nanocomposites, which were synthesized by incorporating CaONPs and DSAC on the surface of GO, were characterized by a significant specific surface area of 733.09 and 709.23 m^2/g, substantial pore volume of 0.201 and 0.199 cm^3/g, and effective pore diameter of 11.09 and 8.21 nm, respectively. The BET curve results suggest that

the GO@CaONPs-ES/DSAC and GO@CaONPs-FB/DSAC nanocomposites (see Fig. S2(e-f)) possessed mesoporous structures (Hosseini et al., 2022). These composites offer an increased surface area and additional active sites for pollutant adsorption compared to the individual constituents.

Table 3. Textural properties

Samples	BET surface area (m^2/g)	Pore volume (cm^3/g)	Pore diameter (nm)
DSAC	698	0.165	5.88
GO	83	0.0303	3.48
CaONPs-ES	62	0.00311	4.90
CaONPs-FB	47	0.00551	4.55
GO@CaONPs-ES/DSAC	733	0.201	11.09
GO@CaONPs-FB/DSAC	709	0.199	8.21

3.1.7 XPS analysis

The XPS analysis was employed to determine the chemical state, elemental oxidation state, and surface composition of the developed GO@CaONPs-ES/DSAC, and GO@CaONPs-FB/DSAC. XPS survey spectrum presented in Fig. 4(a-b) revealed that the GO@CaONPs-ES/DSAC, and GO@CaONPs-FB/DSAC composites are mainly composed of carbon, oxygen, and calcium elements without no impurities detected. GO@CaONPs-ES/DSAC, and GO@CaONPs-FB/DSAC nanocomposites were seen to have exhibited peaks corresponding to only calcium, oxygen and carbon (Chandraraj and Xavier, et al., 2023). The high-resolution spectra of C 1s of GO@CaONPs-ES/DSAC is as shown in Fig. 4(c) reveals two peaks at 284.5 eV and 286.8 eV assigned respectively to C-C and C-O bonds (Jia et al., 2023). The C 1s resolution spectra for GO@CaONPs-FB/DSAC as shown in Fig. 4(d), deconvoluted into three obvious peaks located at 284.4, 285.9, and 288.8 eV assigned to C-C, C-H, and C=O bonds, respectively (Huang et al., 2022b). The presence of C-C, C-O, C-H, and C-H bonds in GO@CaONPs-ES/DSAC, and GO@CaONPs-FB/DSAC composites, suggests the existence of oxygenated functional groups (Ndagijimana et al., 2022b). The GO@CaONPs-ES/DSAC fitting results of O 1 s is depicted in Fig. 4(e). The O-C=O peak located at 531.9 eV suggest the enhanced stability of the composite material. The peak at 536.7 eV could be as a result of the O 1s satellite feature (C=O) (Thombare et al., 2022). The O 1s high-resolution spectra of GO@CaONPs-FB/DSAC presented in Fig. 4(f), shows peaks at 533.9 and 534.7 eV attributable to C-OH and C-O bonds as a result of carbon skeleton residual functional groups (Xu et al., 2022b). The Ca 2p high-resolution spectra of GO@CaONPs-ES/DSAC GO@CaONPs-FB/DSAC composites depicted in Fig. 4(g-h), deconvoluted into two peaks at 347.4 (Ca $2p_{3/2}$) and 351.0 eV (Ca $2p_{1/2}$), suggesting the formation of Ca-O and Ca-OH (Kumar et al., 2022; Ding et al., 2022).

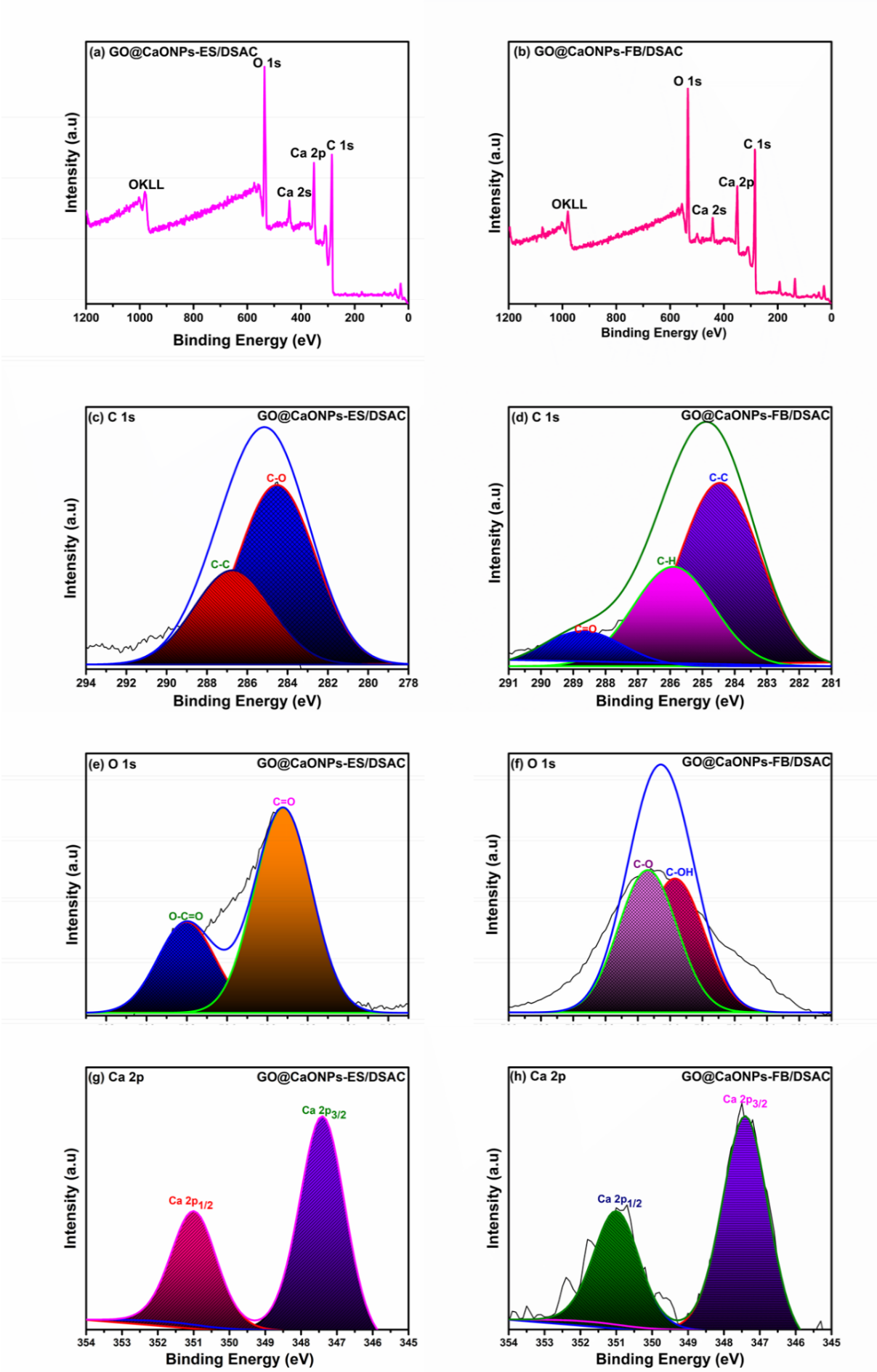
(a) GO@CaONPs-ES/DSAC
O 1s
Ca 2p
C 1s
OKLL
Ca 2s
Intensity (a.u)
1200 1000 800 600 400 200 0
Binding Energy (eV)
(b) GO@CaONPs-FB/DSAC
O 1s
C 1s
Ca 2p
OKLL
Ca 2s
Intensity (a.u)
1200 1000 800 600 400 200 0
Binding Energy (eV)
(c) C 1s
GO@CaONPs-ES/DSAC
C-O
C-C
Intensity (a.u)
294 292 290 288 286 284 282 280 278
Binding Energy (eV)
(d) C 1s
GO@CaONPs-FB/DSAC
C-C
C-H
C=O
Intensity (a.u)
291 290 289 288 287 286 285 284 283 282 281
Binding Energy (eV)
(e) O 1s
GO@CaONPs-ES/DSAC
C=O
O-C=O
Intensity (a.u)
(f) O 1s
GO@CaONPs-FB/DSAC
C-O
C-OH
Intensity (a.u)
(g) Ca 2p
GO@CaONPs-ES/DSAC
Ca 2p3/2
Ca 2p1/2
Intensity (a.u)
354 353 352 351 350 349 348 347 346 345
Binding Energy (eV)
(h) Ca 2p
GO@CaONPs-FB/DSAC
Ca 2p3/2
Ca 2p1/2
Intensity (a.u)
354 353 352 351 350 349 348 347 346 345
Binding Energy (eV)

571

Fig. 4. Full survey scan (a-b), C 1s spectrum **(c-d),** O 1s spectrum **(e-f), and (g-h)** Ca 2p spectrum for GO@CaONPs-ES/DSAC, and GO@CaONPs-FB/DSAC nanocomposites.

3.1.8 Zeta-potential measurement

The charge characteristics of an adsorbent have a significant impact on the adsorption performance. In this study, the surface charge of GO@CaONPs-ES/DSAC and GO@CaONPs-FB/DSAC composites were investigated by Zeta potential measurement at various pH adjustments, as depicted in Fig. 5(a-b). It was clearly observed that GO@CaONPs-ES/DSAC and GO@CaONPs-FB/DSAC composites had a Zeta potential of 32.33 and 22.45 mV at pH 3 and 4 and -17.23 and -12.56 mV at pH 4 and 6, respectively. Therefore, the point of zero charge (PZC) of GO@CaONPs-ES/DSAC and GO@CaONPs-FB/DSAC, determined using linear approximation between the two points for each adsorbent, was 3.42 and 5.04, respectively. This suggests that the surfaces of GO@CaONPs-ES/DSAC and GO@CaONPs-FB/DSAC were positively charged at pH values below 3.42 and 5.04, and negatively charged at pH values above 3.42 and 5.04. Therefore, the positively charged surfaces of the developed adsorbents can be attributed to the abundance of acidic functional groups present (Saeed et al., 2022). Additionally, the adsorbents' surface charge measured after MB adsorption revealed that the PZC of GO@CaONPs-ES/DSAC increased from 3.41-5.91 and that of GO@CaONPs-FB/DSAC increased from 5.04-6.06. This suggests a strong electrostatic interaction and inner-sphere complexes formed between the MB dye and the developed adsorbent (Yu et al., 2021). This indicates that the positively charged surface of the developed adsorbents interacts strongly with the negatively charged MB dye, leading to a noteworthy increase in the adsorption efficiency of the adsorbent.

3.2 Adsorptive performance

3.2.1 Effect of contact time and MB concentration

The equilibrium batch adsorption tests of MB dye onto GO@CaONPs-ES/DSAC, and GO@CaONPs-FB/DSAC were conducted to determine the impact of contact time and initial MB dye concentration on the adsorption capacity at 10-50 mg/L initial MB concentration, solution pH of 8, 0.3 g/L adsorbent dosage, and temperatures of 298-318 K as depicted in Fig. 5(c-h). It was discovered from the plots that the relationship between the adsorption capacity and contact time involves two stages. During the first stage, a rapid increase in MB adsorption onto the developed composites was noticed within the first 60 min, and gradually attains equilibrium position after 60 min at the second stage. The rapid increase in MB adsorption during the earlier stage could be attributed to the availability of more vacant sites and strong electrostatic interaction between negatively charged GO@CaONPs-ES/DSAC, and GO@CaONPs-FB/DSAC surfaces and cationic MB molecules (Thanh et al., 2022). However, as the time increases beyond 60 min, nearly all the MB molecules are binded to the adsorbent active sites, thereby resulting in no significant adsorption capacity (Jawad et al., 2023). Furthermore, an increase in initial MB concentration (10-50 mg/L)

for all the temperatures studied (298-318 K) resulted in an increase in the adsorption capacities of MB dye molecules onto GO@CaONPs-ES/DSAC, and GO@CaONPs-FB/DSAC but adsorption equilibrium was more rapidly attained at lower dye concentration than for higher concentrations (Gaayda et al., 2022). It was observed from the results as presented in Fig. 5(c-h), that as the initial MB dye concentration increases from 10-50 mg/L, the adsorption capacities of MB onto GO@CaONPs-ES/DSAC were increased from 117.7-413.8 mg/g at 298 K, 119.8-436.1 mg/g at 308 K, and 122.8-457.0 mg/g at 328 K, while the adsorption capacities of MB onto GO@CaONPs-FB/DSAC were increased from 112.1-410.3 mg/g at 298 K, 113.4-421.5 mg/g at 308 K, and 121.1-442.4 mg/g at 328 K. Therefore, adsorption capacity increased with increased initial MB concentration, and this can be credited to the driving force increase caused by established gradient between the MB molecules and the adsorbent surfaces (Ahsani-Namin et al., 2022).

3.2.2 Effect of pH solution

The pH of the aqueous solution is significant to the wastewater treatment process because industrial wastewaters possess a wide range of pH values. Furthermore, the pH of the aqueous media can change the surface charge and ionisation of the adsorbents, and subsequently the interaction mechanism between the adsorbates and adsorbents. The effect of pH was investigated on MB adsorption onto GO@CaONPs-ES/DSAC, and GO@CaONPs-FB/DSAC by varying pH between 2-11 at initial MB concentration of 50 mg/L, adsorbent dosage of 0.3 g/L, and contact time of 60 min at temperature of 318 K. A careful observation of the plots depicted in Fig. 6(a-b), revealed that higher percentage removal and adsorption capacity of MB was observed at higher pH solution. The percentage removal and adsorption capacity of MB onto GO@CaONPs-ES/DSAC at pH 2 was 67.9 % and 348.1 mg/g and at pH 8 was 99.2 % and 512.2 mg/g. Similarly, the percentage removal and adsorption capacity for GO@CaONPs-FB/DSAC onto MB at pH 2 was 64.5 % and 330.5 mg/g and at pH 8 was 98.5 % and 505.1 mg/g. The significant increases in percentage removal and adsorption capacity as a function of pH suggested that surface charge might be fundamental to the adsorption process (Dahlan et al., 2023). Electrostatic interactions have previously accounted for variation in MB molecules with MOF adsorbents as a function of pH (Yu et al., 2021). The lower percentage removal and adsorption capacity of MB on both adsorbents can be accredited to the fact that at lower pH ($pH < pH_{PZC}$), the surface of the adsorbents were positively charged, thereby promoting electrostatic repulsion between positively charge cationic MB and the adsorbents (Kumari et al., 2023). The GO@CaONPs-ES/DSAC, and GO@CaONPs-FB/DSAC surfaces become negatively charged at higher pH ($pH < pH_{PZC}$) due to the presence of functional groups such carbonyl and hydroxyl groups. Subsequently, at high pH attractive electrostatic interactions between the adsorbents and positively charged cationic MB exist, resulting in a remarkable adsorption of MB molecules (Ahmadijokani et al., 2023). However, the presence of π-π stacking

between the aromatic ring of MB molecules and that of GO as well as the formation of hydrogen bonds between N atoms of MB molecules and H atoms of hydroxyl, carboxyl, and epoxy groups of GO@CaONPs-ES/DSAC, and GO@CaONPs-FB/DSAC nanocomposites can be attributed to the manifest of adsorption properties even at low pH values. Therefore, this suggests that other mechanisms besides electrostatic attraction also play a role in the interfacial interactions that take place during the adsorption process (Rostamian et al., 2022).

3.2.3 Effect of dosage

In this study, the effect of synthesized GO@CaONPs-ES/DSAC, and GO@CaONPs-FB/DSAC nanocomposites dosage on MB percentage removal and adsorption was investigated and presented in Fig. 6(c-d) The adsorbent dosage was investigated by varying the dosage from 0.1-0.6 g/L at constant initial MB concentration (50 mg/L), pH (8), and constant time (60 min) at temperature (318 K). It was observed that the percentage removal improved and the adsorption loading decreased drastically as the GO@CaONPs-ES/DSAC, and GO@CaONPs-FB/DSAC dosage was increased from 0.1-0.3 g/L, and further increase beyond this point (>0.3 g/L) resulted in no significant additional MB removal. For instance, the percentage removal of GO@CaONPs-ES/DSAC and GO@CaONPs-FB/DSAC increased from 73.1% to 100 %, and 71.1 % to 99.8 %, respectively. The significant increase in the percentage removal with adsorbent dosage increment was attributed to the availability of more active adsorption sites and surface area on the adsorbent surface as the adsorbent dosage was increased (Hadadi et al., 2023). Furthermore, a significant decrease in the adsorption loading from 374.9 mg/g to 170.8 mg/g and 366.0 mg/g to 17.6 mg/g were observed as the GO@CaONPs-ES/DSAC GO@CaONPs-FB/DSAC dosage was increased from 0.1-0.3 g/L. This phenomenon can be explained by the fact that less dye solution was able to bind to the sites at certain dye solution concentrations due to the availability of more adsorptive sites at higher adsorbent dosage (Joshiba et al., 2022).

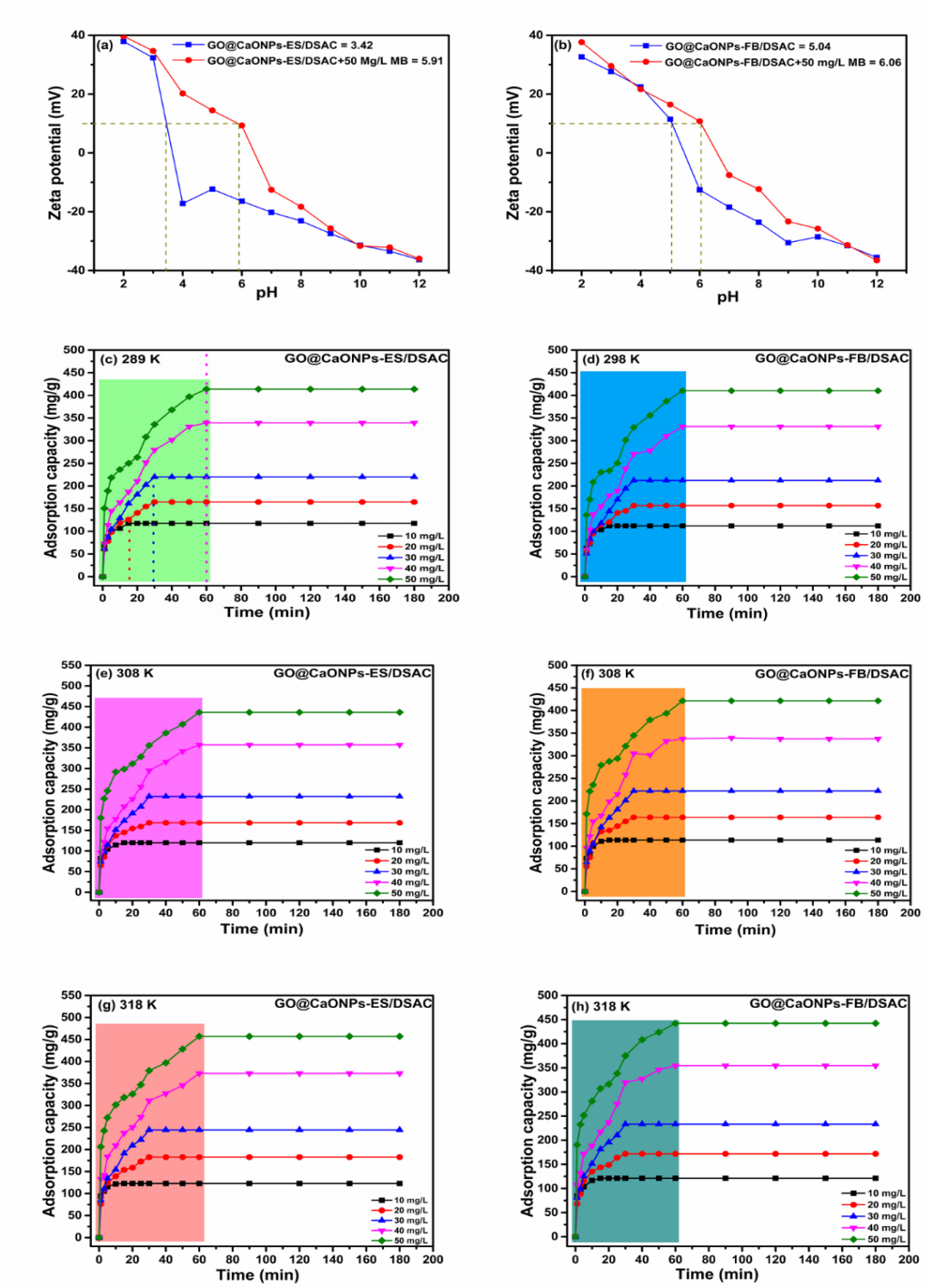

Fig. 5. Zeta-potential measurement (a-b), and effect of contact time and initial concentration at 298 K (c-d), 308 K (e-f), and 318 K (g-h) for GO@CaONPs-ES/DSAC, and GO@CaONPs-FB/DSAC composites.

3.2.4 Effect of temperature

Owing to the fact that the majority of textile dye effluents are released at relatively high temperatures, temperature is a key variable in the applications of the proposed adsorptive dye removal process. The effect of temperature was examined in a varying reaction temperature of 298-338 K, at equilibrium conditions of initial MB concentration of 50 mg/L, adsorbent dosage of 0.3 g/L, pH 8, and contact time of 60 min. The results presented in Fig. 6(e-f), revealed that the percentage removal and adsorption capacities of MB onto GO@CaONPs-ES/DSAC

GO@CaONPs-FB/DSAC composites increased significantly with increased in increasing temperature, suggesting that the adsorption process is endothermic in nature. In addition, percentage removal and adsorption capacity increase of MB on GO@CaONPs-ES/DSAC GO@CaONPs-FB/DSAC as the reaction temperature increases could be attributed the greater mobility, improved degree of solubility and dissociation of MB molecules which result in more collisions and accelerate binding of the MB molecules into the adsorptive sites of the adsorbents (Gurav et al., 2022).

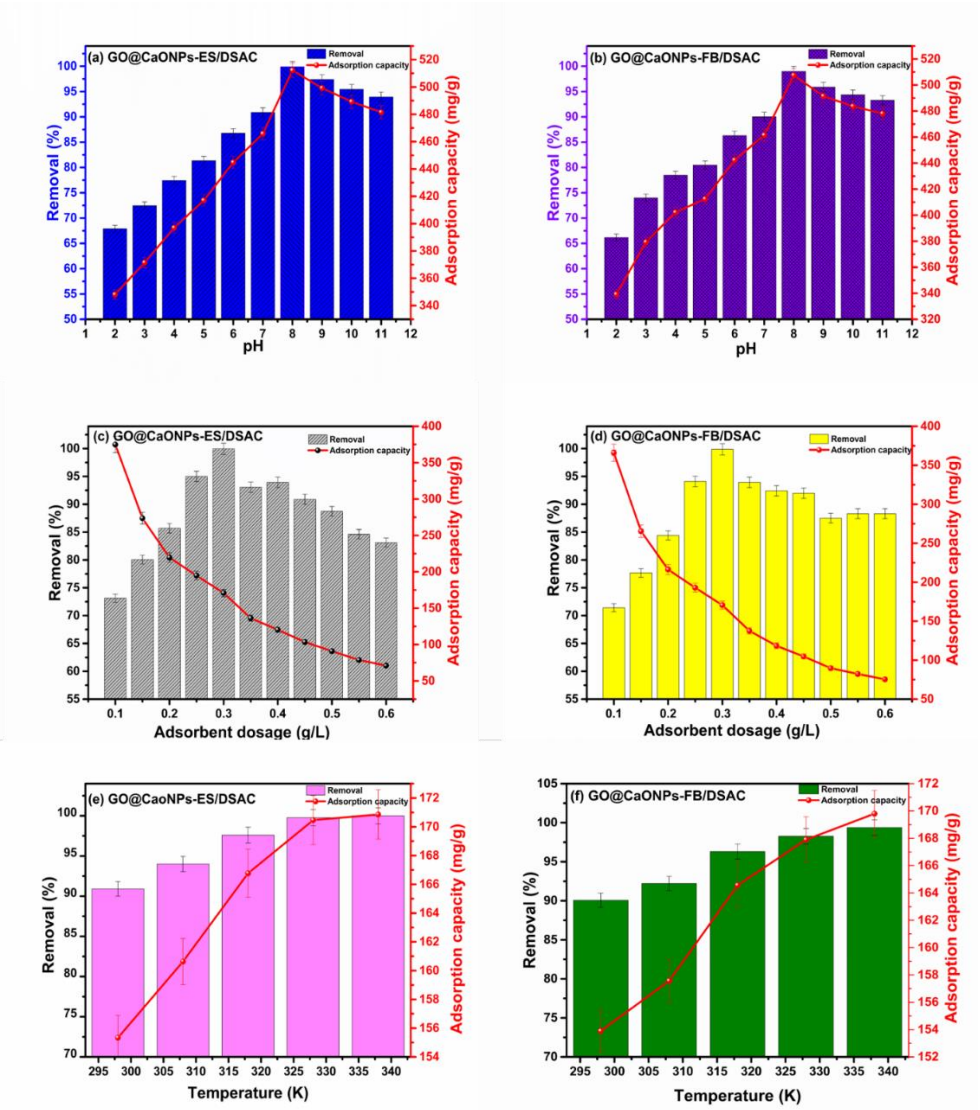

Fig. 6. Effect of pH (a-b), adsorbent dosage (c-d), and temperature (e-f) for GO@CaONPs-ES/DSAC, and GO@CaONPs-FB/DSAC composites.

3.3 Adsorption isotherm

The ability an adsorbent to adsorb toxic dye compounds is determined by the adsorption isotherm experiment. It is also employed to investigate how the adsorbent and the pollutant interact, and it also aids in explaining how the adsorbates are distributed and interacts with the liquid and solid phases when they are in equilibrium, adsorbent energetic properties, and nature of coverage. In order to understand the adsorptive behaviour of MB dye onto GO@CaONPs-ES/DSAC and GO@CaONPs-FB/DSAC, the adsorption experimental data was fitted to eight models, namely; Langmuir, Freundlich, Temkin, Dubinin and Radushkevich, Jovanovic, Harkins-Jura, Halsey, and

Redlich-Peterson and their linear form of equations is summarized in Table S1-S2. The adsorption isotherm model plots, their corresponding parameters, correlation of coefficient (R^2) and error functions obtained from the linear plots are presented in Fig. S3(a-h) and Table 4. Langmuir isotherm assumes the existences of monolayer coverage of the adsorbates at the outer surface of the adsorbent where all adsorption sites are identical. The Freundlich isotherm assumes a heterogeneous adsorption surface with non-uniform distribution of affinity and sorption heat. Temkin model considered the interactions between the adsorbate and adsorbent. The model assumes that the distribution of binding energies is uniform and that the heat of adsorption of all molecules in the layer diminishes linearly with coverage. The Dubinin-Radushkevich model assumes the mechanism of adsorption has a Gaussian energy distribution on the adsorbent heterogeneous surface; this model also provides insight into the nature of adsorption process, whether chemical, ion-exchange, or physical. The Jovanovic model is based on the same assumptions as the Langmuir model, but it also considers the potential of certain mechanical interactions between the adsorbent and adsorbate. The Harkin-Jura isotherm model assumes that multilayer adsorption might occur on the surface of absorbents with a heterogeneous pore distribution. The Halsey model is employed for multilayer adsorption at a distance from the surface that is relatively large, and the adsorbent is heterogeneous in nature. The Redlich-Peterson model deviates from ideal monolayer adsorption because it is a hybrid isotherm that combines the Langmuir and Freundlich isotherms.

Centred on the high correlation of coefficient value (R^2), reduced sum of square errors and Hybrid fractional error function (HYBRID) as tabulated in Table 4, the adsorption of MB dye onto GO@CaONPs-ES/DSAC was better fitted to the Freundlich model, suggesting that the sorption process followed a heterogeneous surface with multilayer adsorption mechanism. This also implies that the surface's heterogeneity was associated with a number of adsorbent-adsorbate interactions as well as the availability of various functional groups on the surface (Debnath and Das et al., 2023). The parameter 1/n provides information on the degree of surface heterogeneity, with values between 0 and 1 suggesting greater surface heterogeneity as the value approaches zero (Kim et al., 2023). The 1/n values calculated for GO@CaONPs-ES/DSAC at different temperature were 0.85, 0.82 and 0.75 respectively, demonstrated that the adsorption surface of GO@CaONPs-ES/DSAC was heterogeneous in nature. Similarly, the experimental data of MB adsorption onto GO@CaONPs-FB/DSAC based on the high R^2, small SSE and HYBRID values was observed to be best described by the Harkins-Jura model, demonstrating the presence of multilayer adsorption mechanism and heterogeneous pore surface distribution (Zhu et al., 2023). The Harkins-Jura model is also similar to the Freundlich model. Moreover, Dubinin–Radushkevich and Temkin models suggested that the adsorption of MB dye onto GO@CaONPs-ES/DSAC and GO@CaONPs-FB/DSAC is physical in nature (b_T and $E < 8$kJ/mol) as a result of the electrostatic interaction between the opposing charges

present in the MB dye and adsorbents (Sellaoui et al., 2023). During physical adsorption process, the MB dye attached to the adsorbents through a weak van der Waals interaction; as a result, this mechanism is related to relatively low adsorption energies. It is therefore established that GO@CaONPs-ES/DSAC and GO@CaONPs-FB/DSAC are heterogeneous in nature and that multiple mechanisms are involved in the overall adsorption (Abutaleb et al., 2023). The Temkin model b_T values calculated for both adsorbents indicates that the adsorption process is endothermic in nature (b_T <1000 J/mol) (Adedeji and Jahan, 2023). The maximum MB adsorption capacities calculated from the Langmuir model at different temperatures (298, 308, and 318 K) were 1062.78, 1199.56, and 1274.48 mg/g for GO@CaONPs-ES/DSAC, and 621.12, 684.93, and 689.66 mg/g for GO@CaONPs-FB/DSAC, respectively. The increased adsorption capacities as the temperature is increased also support the endothermic nature of the adsorption process. These findings also demonstrated that the GO@CaONPs-ES/DSAC that has a better uptake capacity than GO@CaONPs-FB/DSAC owing to its active binding sites and higher surface area. Furthermore, the heterogeneous nature and multilayer adsorption mechanism for both adsorbents were further supported by the Halsey (R^2 values closer to 1, small SSE and HYBRID values), and Redlich-Peterson (β_{RP} values are less than 1, suggesting that the adsorption process is more suitably explained by Freundlich model) models (Lin et al., 2022). In conclusion, the MB adsorption experimental data is fitted in the following order;

GO@CaONPs-ES/DSAC: Freundlich > Hasley > Temkin > Jovanovic > Harkin-Jura > Dubinin–Radushkevich > Redlich-Peterson > Langmuir.

GO@CaONPs-ES/DSAC: Harkins-Jura > Freundlich > Halsey > Jovanovic > Redlich-Peterson > Temkin > Langmuir > Dubinin–Radushkevich.

Table 4. Adsorption model parameters of GO@CaONPs-ES/DSAC and GO@CaONPs-FB/DSAC.

Isotherms	Parameters	GO@CaONPs-ES/DSAC			GO@CaONPs-FP/DSAC		
		298	308	318	298	308	318
Langmuir	Q_m (mg/g)	1062.78	1199.56	1274.48	621.12	684.93	689.66
	K_L (L/mg)	0.027	0.034	0.061	0.090	0.096	0.12
	R^2	0.938	0.851	0.840	0.845	0.825	0.868
	SSE	260.89	3320.22	4478.60	1.35	1.33	1.12
	HYBDRID	55.68	39.98	33.88	5.69	3.61	2.67
Freundlich	K_F (mg/g) $(L/mg)^{1/n}$	36.29	48.55	71.36	73.59	82.61	97.25
	1/n	0.85	0.82	0.75	0.58	0.59	0.58
	R^2	0.994	0.996	0.989	0.967	0.969	0.973
	SSE	0.0000063	0.000012	0.000014	0.013	0.012	0.011
	HYBDRID	1.67	1.35	1.12	0.99	0.60	0.40
Temkin	K_T (L/mg)	0.50	0.71	1.00	1.24	1.35	1.65
	b_T (J/mol)	15.27	16.018	16.086	20.57	20.62	21.59

	R^2	0.996	0.965	0.961	0.927	0.918	0.929
	SSE	0.0093	0.0090	0.025	0.37	0.36	0.39
	HYBDRID	5.67	3.67	2.79	0.99	1.23	0.90
Dubinin–Radushkevich (D-R)	q_s (mg/g)	291.33	305.65	312.31	260.72	278.98	290.56
	K_{ad} (mol^2/J^2) 10^{-7}	31.33	12.68	6.96	6.00	4.80	3.34
	E (kJ/mol)	0.40	0.63	0.85	0.91	1.021	1.22
	R^2	0.971	0.901	0.871	0.811	0.818	0.809
	SSE	0.46	0.22	0.28	6447.89	8256.69	8265.11
	HYBDRID	25.69	22.90	20.56	20.223	19.456	15.676
Jovanovich	$q_{m,\,Jv}$ *(mg/g)*	77.41	82.22	89.71	92.726	94.374	102.888
	K_{Jv} *(L/g)*	-0.11	-0.14	-0.17	-0.108	-0.134	-0.143
	R^2	0.954	0.981	0.985	0.978	0.933	0.986
	SSE	0.0093	0.0090	0.025	0.000093	0.000063	0.000036
	HYBDRID	10.11	9.69	11.34	0.068	0.055	0.051
Harkins-Jura	A_{HJ} (g^2/L)	6990.76	6899.45	9587.82	10321.29	11361.067	12942.77
	B_{HJ} (mg^2/L)	1.12	1.024	0.96	1.14	1.073	1.018
	R^2	0.907	0.964	0.970	0.983	0.992	0.990
	SSE	0.075	0.044	0.035	1.85×10^{-10}	6.80×10^{-11}	7.34×10^{-11}
	HYBDRID	17.90	15.32	11.90	0.0034	0.0011	0.021
Halsey	K_H (mg/L)	69.52	117.43	288.99	1632.45	1717.16	2669.78
	n_H	1.18	1.22	1.33	1.72	1.69	1.72
	R^2	0.994	0.996	0.989	0.967	0.969	0.973
	SSE	0.0018	0.0017	0.0047	0.041	0.035	0.014
	HYBDRID	1.90	1.80	1.71	0.99	0.85	0.55
Redlich-Peterson	β_{RP}	0.15	0.18	0.25	0.42	0.41	0.42
	A (L/g)	36.29	48.55	71.36	73.59	82.61	97.25
	R^2	0.861	0.930	0.912	0.939	0.938	0.950
	SSE	12.34	8.68	5.013	0.048	0.036	0.021
	HYBDRID	34.57	29.90	29.55	1.12	1.045	1.022

Table 5. Kinetics adsorption parameters of GO@CaONPs-ES/DSAC and GO@CaONPs-FB/DSAC nanocomposites towards MB

Models	Parameters	GO@CaONPs-ES/DSAC					GO@CaONPs-FB/DSAC				
		10	20	30	40	50	10	20	30	40	50
PFO	$q_{e\ exp}$	12.32	18.49	27.34	40.61	51.26	12.32	18.49	27.34	40.61	51.26
	$q_{e\ cal}$	9.96	13.77	19.37	32.55	41.096	9.38	14.60	19.66	37.97	45.91
	k_1 (min^{-1})	0.13	0.10	0.067	0.077	0.068	0.15	0.15	0.068	0.093	0.085
	R^2	0.986	0.940	0.992	0.993	0.991	0.980	0.974	0.993	0.968	0.980
	SE	0.10	0.20	0.059	0.0031	0.0031	0.15	0.19	0.057	0.20	0.14
PSO	$q_{e\ exp}$	12.32	18.49	27.34	40.61	51.26	12.32	18.49	27.34	40.61	51.26
	$q_{e\ cal}$	11.25	16.44	22.22	38.58	48.84	11.49	17.47	28.21	39.87	50.94
	k_2 (g mg min^{-1})	0.0049	0.0018	0.00068	0.00038	0.00023	0.0058	0.0028	0.00067	0.00042	0.00031
	R^2	1.000	0.999	0.999	0.999	0.999	0.999	0.999	0.999	0.999	0.999
	SE	0.0034	0.0054	0.0041	0.0035	0.0034	0.0030	0.0037	0.0039	0.0029	0.0024
Elovich	α (mg $g^{-1}min^{-1}$)	323.19	121.75	93.33	99.53	96.29	522.36	216.59	93.33	116.68	142.15
	β (g/mg)	0.067	0.044	0.026	0.0166	0.013	0.070	0.047	0.025	0.017	0.013
	R^2	0.912	0.938	0.962	0.958	0.963	0.904	0.920	0.966	0.962	0.962
	SE	6.59	8.23	10.88	17.62	21.72	6.62	8.93	10.33	16.67	21.55
Intraparticle-diffusion	k_{ip} (mg g^{-1} min-$^{0.5}$)	4.56	7.41	13.37	20.67	27.53	4,32	6.69	13.44	20.45	26.54
	C	65.40	65.093	76.92	95.28	96.98	70.36	76.77	77.14	105.52	131.55
	R^2	0.719	0.788	0.845	0.847	0.869	0.705	0.741	0.848	0.845	0.847
	SE	8.93	11.73	17.17	26.30	31.79	8.79	12.28	17.022	26.24	33.78
Boyd	B	0.13	0.10	0.066	0.078	0.068	0.15	0.15	0.067	0.095	0.087
	D_i (10^{-11} m^2/s)	5.55	4.89	3.32	4.89	4.12	3.43	4.21	5.66	5.89	6.10
	R^2	0.986	0.927	0.991	0.992	0.990	0.977	0.969	0.992	0.965	0.98
	SE	0.12	0.26	0.069	0.089	0.087	0.18	0.25	0.067	0.23	0.17

3.4 Adsorption kinetics

The kinetic examination for a specific adsorption system is essential for understanding the pathways and mechanism that governs the MB adsorption process. The adsorption kinetics also define the rate of adsorption, which establishes the amount of time needed for the adsorption process to attain equilibrium. The adsorption process and accessibility to the adsorption sites at the solid-liquid interface are related to surface site interactions, pore and surface diffusion, eternal diffusion, and bulk diffusion which may involves physical or chemical adsorption (Kojo et al., 2022). The experimental data of MB on GO@CaONPs-ES/DSAC and GO@CaONPs-FB/DSAC were fitted to the elovich, Boyd, pseudo- first order (PFO), intraparticle-diffusion and pseudo-second order (PSO) models, and to understand the mechanism of adsorption. The kinetic model equations are summarized in Table S1-S2 and the linear fitting plots are presented in Fig. S4(a-e).

The PFO, PSO and elovich kinetic model parameters presented in Table 5, reveal that the three tested models well explained the adsorption process. However, the PSO best described the character of MB adsorption onto GO@CaONPs-ES/DSAC and GO@CaONPs-FB/DSAC based on the higher R^2 (closer to unity), and the small standard errors (SE) values. When compared to PFO, the experimental adsorption capacities for PSO were found to be closer to the calculated adsorption capacities at different concentrations (Khnifira et al., 2023). The elovich model parameter values revealed that both the sorption rate and the desorption rate gradually decreased as the starting concentration of dyes increased. The adsorption process' feasibility was demonstrated by a greater α values, identifying a higher adsorption rate than desorption (Kim et al., 2023).

The intraparticle-diffusion curve in Fig. S4(d) for MB adsorption onto GO@CaONPs-ES/DSAC and GO@CaONPs-FB/DSAC shows two separate stages; the steep and the linear. At the steep side, the majority of the MB was quickly adsorbed on the external surfaces of GO@CaONPs-ES/DSAC and GO@CaONPs-FB/DSAC due to the high rate of mass transfer in the diffusion boundary layer. However, for the second stage (linear stage) once the external adsorption sites were full, the adsorption process was slowed down by the slower intra-particle diffusion rate of MB (Abutaleb et al., 2023). In other words, the two stages associated with the uptake of MB dye onto GO@CaONPs-ES/DSAC and GO@CaONPs-FB/DSAC are; (1) fast adsorption on the external surfaces of the adsorbents, and (2) intra-particle diffusion and final equilibrium state (Lin et al., 2022). Additionally, the intraparticle diffusion constant, C increases as the initial MB dye concentration increases, demonstrating a resistance to the concentration gradient across the adsorbent surfaces (Abdoul et al., 2023). However, the

intraparticle-diffusion plots for both adsorbents did not cut across the origin, which indicates that during the adsorption process, the intraparticle-diffusion is not the only step for determining the rate of the reaction (Du et al., 2023). Hence, it can be predicted that the intraparticle diffusion and external mass transfer and may work together simultaneously in MB dye adsorption. The Boyd plots for GO@CaONPs-ES/DSAC and GO@CaONPs-FB/DSAC depicted in Fig. 10(e) clearly show that the straight line's divergence from the point of origin, indicating that the external mass transfer or film diffusion, rather than particle diffusion, is the dominant mechanism (Joshiba et al., 2022).

3.5 Adsorption thermodynamics

Adsorption isotherms which are temperature-dependent allow us to estimate the adsorption process by calculating the enthalpy change (DH^o), standard free-energy change (DG^o), and entropy change (DS^o) via the given equations.

$$\Delta G = \Delta G^o + RT \ln K^o_{Equilibrium} \quad (9)$$

Since, the free energy change (ΔG) becomes negligible as the adsorption process attains equilibrium, Equ. 1 therefore becomes;

$$-\Delta G^o = RT \ln K^o_{Equilibrium} \quad (10)$$

The affiliation between ΔG^o, ΔS^o and ΔH^o can be described as:

$$\Delta G^o = \Delta H^o - T\Delta S^o \quad (11)$$

Combining Equ. 4 and 5, and making $\ln K^o_{Equilibrium}$ subject of the formula, we have the Van't Hoff expression;

$$\ln K^o_{Equilibrium} = -\frac{\Delta H^o}{RT} + \frac{\Delta S^o}{R} \quad (12)$$

$$K^o_{Equilibrium} = \frac{(K_L \times M_w \times 1000) \times [C^o]}{\gamma} \quad (13)$$

where $K^o_{Equilibrium}$ is the thermodynamic equilibrium constant (dimensionless), M_w stands for the MB molecular weight (319.85 g/mol), K_L represents the Langmuir constant, K_L (L/mg), γ is the coefficient activity of MB in solution (dimensionless) and [C]° is the standard concentration of the MB (1 mol/L). Since the MB dye solution is very diluted, the activity of coefficient (γ) is considered unitary.

The adsorption activation energy was employed further to confirm the adsorption character of MB dye by GO@CaONPs-ES/DSAC and GO@CaONPs-FB/DSAC using the Arrhenius equation as given by;

$$\ln k_2 = -\frac{E_a}{R}\left(\frac{1}{T}\right) + \ln A \quad (14)$$

where E_a is adsorption activation energy (kJ/mol), A corresponds to the Arrhenius constant, and k_2 is the rate constant for the pseudo-second order.

The E_a values were derived from the intercept and slope $\ln k_2 \; against \; \frac{1}{T}$ plots. (plots not shown). The value of E_a between 5-40 kJ/mol suggest physical mechanism while the value from 40-80 kJ/mol reveal a chemical mechanism. The values of ΔS^o and ΔH^o were obtained from the slope and intercept of $\ln K^o_{Equilibrium}$ versus 1/T as presented in Fig. 7(a-b). The results of the thermodynamics for MB dye adsorption on GO@CaONPs-ES/DSAC and GO@CaONPs-FB/DSAC are tabulated in Table 6. The negative value of ΔG^o calculated at all temperatures for both adsorbents, implies that adsorption is a spontaneous process. feasible to adsorb MB onto GO@CaONPs-ES/DSAC and GO@CaONPs-FB/DSAC (Luo et al., 2023).The positive values of ΔH^o and ΔS^o revealed the endothermic nature and randomness increase at the adsorbate-adsorbent interface during the adsorption process of MB resulting in degree of freedom increased (Yang et al., 2022). The high ΔS^o values revealed that the adsorbents have a strong affinity with MB dye during the adsorption process (Kojo et al., 2022). The ΔG^o values for GO@CaONPs-ES/DSAC and GO@CaONPs-FB/DSAC was discovered to have increased as the reaction temperature was raised, indicating that the adsorption process was endothermic. The ΔH^o values of 30.47 and 11.62 kJ/mol which were less than 40 kJ/mol, suggest that the process of sorption of MB dye on GO@CaONPs-ES/DSAC and GO@CaONPs-FB/DSAC is more dominated by a physical adsorption mechanism (Wu et al., 2023). The dominance of physical adsorption mechanism was further supported by the E_a values (5-40 kJ/mol).

Table 6. Thermodynamic parameters

Adsorbent	T (K)	$\ln K^o_{Eq.}$	ΔG^o (kJ mol^{-1})	ΔH^o (kJ mol^{-1})	ΔS^o (J mol^{-1} K^{-1})	E_a (kJ/mol)
GO@CaONPs-ES/DSAC	298	9.067	-22.354	30.47	177.28	14.63
	308	9.29	-24.126			
	318	9.87	-25.899			
GO@CaONPs-FB/DSAC	298	10.26	-25.373	11.62	124.15	10.23
	308	10.33	-26.612			
	318	10.57	-27.942			

3.6 Cyclic performance test

In a sustainable application process, recovering and reusing adsorbents is economically essential. The regeneration process was investigated in this study by desorbing MB dye from the surfaces of GO@CaONPs-ES/DSAC and GO@CaONPs-FB/DSAC nanocomposites after adsorption by using 5 % glacial acetic acid in ethanol solution. The mixture of glacial acetic with ethanol is employed to boost the polarity of the solvent in order to break the electrostatic

contact between the adsorbent and adsorbate because MB desorption using simply ethanol is not satisfactory. The sorbents were then dried in an oven after being washed repeatedly with distilled water. The dried adsorbents were tested in a batch equilibrium adsorption cycles on MB dye at optimal conditions. The adsorption-desorption cycle of MB dye on GO@CaONPs-ES/DSAC and GO@CaONPs-FB/DSAC was repeated 10 times in a similar method. The results illustrated in Fig. 7(c), indicates that in the first cycle, the GO@CaONPs-ES/DSAC and GO@CaONPs-FB/DSAC nanocomposites produced effectively the removal of 98.89 and 96.45 %, respectively. However, after the tenth successive cycle of GO@CaONPs-ES/DSAC and GO@CaONPs-FB/DSAC nanocomposites, the MB removal decreased slightly to 96.45 and 85.18 % (< 10 %). The results demonstrated a stable and excellent regeneration ability and reusability of the developed adsorbents in multipurpose applications. Furthermore, GO@CaONPs-ES/DSAC and GO@CaONPs-FB/DSAC nanocomposites may be a sustainable option for adsorptive uptake of dye pollutants and wastewater remediation due to their excellent percentage removal, high stability, rapid adsorption kinetics, and suitability for MB dye removal

3.7 Practical application in real-time wastewater

The present study collected different water samples to test the applicability and adsorption performance of GO@CaONPs-ES/DSAC and GO@CaONPs-FB/DSAC in a real time application. 100 mL of sea water, distilled water, agricultural wastewater, and tap water were collected and measured in several Erlenmeyer flasks (250 mL), and was spiked with MB (50 mg/L). Thereafter, GO@CaONPs-ES/DSAC and GO@CaONPs-FB/DSAC (0.3 g/L of each) was added and the flasks were positioned at constant temperature of 318 K for 60 min on the water bath shaker. The percentage removal of MB on GO@CaONPs-ES/DSAC were 100 %, 100 %, 100 %, and 90.56 % for tap water, agricultural wastewater, distilled water and sea water respectively. Similarly, the MB adsorption on GO@CaONPs-FB/DSAC were 100 %, 99.89 %, 100 %, and 82.78 % for tap water, agricultural wastewater, distilled water and sea water. The decrease in the percentage removal of MB from the sea water could be attributed to the presence of positively charge Mg^{2+} and Ca^{2+}, competing with MB on the surface of the adsorbents, thereby resulting in a decrease of removal.

3.8 Selective Sorption test of MB and other pollutants

The adsorptive performance of GO@CaONPs-ES/DSAC and GO@CaONPs-FB/DSAC nanocomposites towards MB and selected pollutants such as lead (Pb), methylene orange (MO), and Chloroquine phosphate (CQP) were investigated at different pH by introducing 0.3 g/L each of GO@CaONPs-ES/DSAC and GO@CaONPs-FB/DSAC into several Erlenmeyer

flask containing 50 mL each of MB, MO, CQP and Pb (50 mg/L). The flasks were then placed on the magnetic shaker at 318 K for 60 min, and the residual concentration were measured. The results depicted in Fig. 7(d-e), revealed that increased pH resulted in a decrease in the uptake efficiency of MO, while the percentage removal of CQP, MB and Pb were favoured for both adsorbents. The observed increase in percentage removal of MB, Pb, and CQP at higher pH value, could be accredited to the fact that, at higher pH, the surfaces of GO@CaONPs-ES/DSAC and GO@CaONPs-FB/DSAC were deprotonated (negatively charged) due to the presence of $-OH^-$ and -COOH thereby promoting high electrostatic interaction between Pb, CQP, the positively charged MB and the adsorbents. However, at lesser pH, the adsorbents surface is protonated (charged positively) and the adsorption of anionic MO (negatively charged) is favoured due to electrostatic interaction. However, it was discovered that pH 6 resulted in the highest percentage removal of CQP from GO@CaONPs-ES/DSAC and GO@CaONPs-FB/DSAC. This observation may be due the fact that the p*K*a of CQP as reported in previous research was 8.4, suggesting that at pH<8.4, the CQP is cationic (protonated) (Wang et al., 2023). Hence, the CQP adsorption was observed to be promoted by the negatively charged GO@CaONPs-ES/DSAC (pH >3.42) and GO@CaONPs-FB/DSAC (pH > 5.54) surfaces. The decrease in the CQP removal onto both adsorbents at pH 8, could be attributed to the significant in the CQP positive charge (reduction to zero) which resulted in weak electrostatic force (Bezerra de Araujo et al., 2023).

3.9 Impact of co-existing ions

The influence of competing ions is an important study in wastewater treatment because natural water and industrial wastewater are usually comparises of various inorganic salts even at higher concentrations, which may influence the MB performance towards the adsorbents. The transformation, migration, and pollutant's bioavailability performance in aqueous environment might be affected by the presence of interfering inorganic salts significantly (cations or anions) with good chemical reactivity and energetic complexation ability towards the MB and the adsorbent surfaces. In this work, the impact of co-existing ions (cations and anions) on MB adsorption onto GO@CaONPs-ES/DSAC and GO@CaONPs-FB/DSAC were tested using 0.01 M ionic salt concentrations of $NaHCO_3$, $NaNO_3$, NaCl, $MgCl_2$, and $CaCl_2$ at optimum conditions (Initial MB concentration is 50 mg/ L, Temperature is 318 K, pH is 8, contact time is 60 min, Adsorbent dosage is 0.3 g/L) as presented in Fig. 7(f).

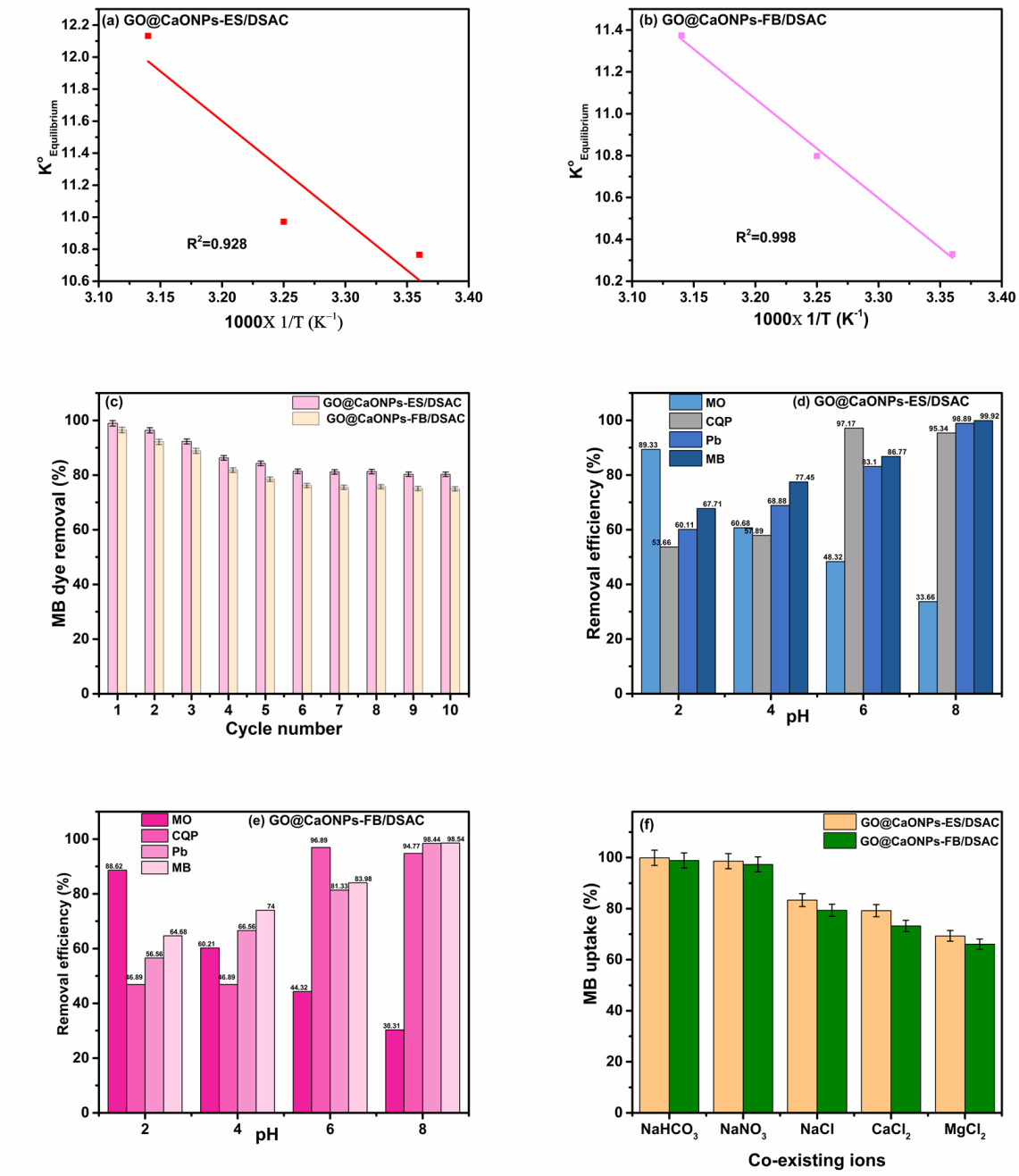

Fig. 7. Plots of (a-b) Thermodynamics curve, (c) reusability study, (d-e) MB dye adsorption with other pollutants, and (f) impact of co-existing ions of MB dye adsorption onto GO@CaONPs-ES/DSAC, and GO@CaONPs-FB/DSAC nanocomposites.

The results confirmed a smooth decrease in the MB dye removal efficiency on GO@CaONPs-ES/DSAC (83.34, 79.23, and 67.32 %) and GO@CaONPs-FB/DSAC (79.34, 73.23, and 66.10 %) with the cations ($Na^+ > Ca^{2+} > Mg^{2+}$). The decrease in MB dye removal could be attributed to the fact that dissolution of NaCl, $MgCl_2$ and $CaCl_2$ salts in aqueous solution releases Na^+, Mg^{2+}, and Ca^{2+}, which compete with cationic MB dye for adsorption on the adsorbents surface. Also, the small ionic radius (0.102 nm Na^+, 0.100nm Ca^{2+}, and 0.072 nm Mg^{2+}) and their chemical valency state may contribute to their restriction on the surfaces of GO@CaONPs-ES/DSAC and GO@CaONPs-FB/DSAC (Zong et al., 2022). Furthermore, the dissolution of

$NaHCO_3$, and $NaNO_3$ in aqueous solution releases HCO_3^- and NO_3^- (anions) which compete with -OH and -COOH on the adsorbent surfaces, increasing the negative charge on the adsorbent surfaces, which strengthens the electrostatic interaction between the negatively charged adsorbents and the positively charged MB dye (Shaikh et al., 2022). Therefore, the inhibitory effect the co-existing ions on MB uptake by GO@CaONPs-ES/DSAC and GO@CaONPs-FB/DSAC nanocomposites follow the order: $Mg^{2+} > Ca^{2+} > Na^+$, $> NO_3^- > HCO_3^-$.

3.10 Comparative study

In this research, MB dyes adsorption capacity towards GO@CaONPs-ES/DSAC and GO@CaONPs-FB/DSAC nanocomposites were compared with other GO-based adsorbents in previous works as presented in Table 7. It was observed clearly that the highest MB adsorption capacities calculated from the Langmuir model for GO@CaONPs-ES/DSAC and GO@CaONPs-FB/DSAC nanocomposites were 1274.5 and 689.7 mg/g, which were significantly greater than those reported for several adsorbents. The superior adsorption capacities of GO@CaONPs-ES/DSAC and GO@CaONPs-FB/DSAC nanocomposites, suggest that the adsorbents can be considered as an effective adsorbent to remediate water polluted with MB.

Table 7. Maximum adsorption capacities for MB dye adsorption by various GO-based nanocomposites

Adsorbent	Optimal conditions	Adsorption capacity (mg/g)	References
MgO/GO	pH 11, 12 min, 308 K	171.9	Guo and Bulin, (2021)
GAC-GO	pH 12, 50 min, 333 K	222.7	Ndagijimana et al., (2021)
PAC-GO	pH 12, 5 min, 333 K	248.1	Ndagijimana et al., (2021)
CS/AAm/IA/GO	pH 8, 90 min, 298 K	247.5	Tamer et al., (2022)
α-MnO2NRs/GO-Chit	pH 7, 24 min, 298 K	328.9	Rajendiran, et al., (2022)
Agar/GO/ZnO	pH 6.5, 40 min, 303K	33.0	Moradi et al., (2022)
FSGOMs	pH 6, 15 min, 298 K	420.0	Narayanam et al., (2022)
GO/CS	pH 5, 125 min, 298 K	7.5	Khiam et al., (2022)
GO-N	pH 7, 15 min, 300 K	311.5	Nizam et al., (2022)
Agar/GO	pH 6.5, 40 min, 303K	81.3	Moradi et al., (2022)
GO-H	pH 7, 15 min, 300 K	288.3	Nizam et al., (2022)
AG-GO-HMTA	pH 5, 300 min, 298 K	168.0	Lotfy et al., (2023)
CS/GO12	pH 8, 120 min, 308 K	259.5	Tran et al., (2023)
GO/SiO_2	pH 8, 30 min, 278 K	555.5	Dan et al., (2023)
Fe_3O_4@GO@AHSA	pH 7, 240 min, 298 K	286.4	Alsohaimi et al., (2023)
GO@CaONPs-FB/DSAC	pH 8, 60 min, 318 K	689.7	This work
GO@CaONPs-ES/DSAC	pH 8, 60 min, 318 K	1274.5	This work

3.12 Mechanism of adsorption

The GO@CaONPs-ES/DSAC and GO@CaONPs-FB/DSAC nanocomposites adsorption performance of could be controlled by various factors including the textural and structural properties, surface material composition, surface chemistry, adsorbate structure and the

adsorbent surface charge. The comparison of the BET examination after and before MB dye uptake revealed a noteworthy decrease in the BET surface area from 733.09 m^2/g to 206.11 m^2/g; for GO@CaONPs-ES/DSAC (71.9 % decrease) and 709.23 m^2/g to 133.21 m^2/g (81.2 % decrease). The pore volume and BET surface area decreased after MB dye adsorption as presented in Table S3, could be accredited to the adsorbed MB dye accumulation on the adsorbent surfaces, signifying that the mechanism of adsorption is led by pore-filling. The results revealed that the MB dye is adsorbed majorly on the internal porosity of the adsorbents (mesoporous in nature).

The FTIR spectra of GO@CaONPs-ES/DSAC and GO@CaONPs-FB/DSAC nanocomposites before and after adsorption is depicted in Fig.8(a). The GO@CaONPs-ES/DSAC spectra before adsorption have peaks at 3641, 3468, 1643, 1416, 1149, and 868 cm^{-1} assigned to O-H, C=O, C-OH, C-O, and Ca-O, respectively. However, after MB adsorption the peaks at 3468, 1643, 1416, and 868 cm^{-1} were captured. The fading of the peak at 3641 cm^{-1} and the appearance of new peak at 2349 cm^{-1} could be attributed to electrostatic interaction, demonstrating the successful capturing of MB dye on the GO@CaONPs-ES/DSAC surface. The FTIR spectra of GO@CaONPs-FB/DSAC displayed peaks before MB adsorption at 3468, 2360, 1630, and 1068 cm^{-1} corresponds to the O-H vibration stretching, C-H, C=C, and C-N groups. Furthermore, after MB dye adsorption all the peaks were observed to be retained with the appearance of a new peak at 1434 cm^{-1} which aligns to the CH_3 symmetrical and asymmetrical bending vibrations of the MB dye. The XRD diffractogram of GO@CaONPs-ES/DSAC and GO@CaONPs-FB/DSAC after and before adsorption is displayed in Fig. 8(b). The results revealed that was no change in the crystal position of GO@CaONPs-ES/DSAC and GO@CaONPs-FB/DSAC, that is no formation and disappearance of diffraction peaks after MB adsorption from the diffractogram when compared, indicating the adsorption process involve physical adsorption mechanism as predicted by the Dubinin-Radushkevich (DR) and Temkin isotherm models However, the shorter and longer diffraction peaks observed after adsorption when compared for GO@CaONPs-ES/DSAC and GO@CaONPs-FB/DSAC, indicates that MB adsorption is successfully adsorbed. The TEM analysis depicted in Fig. 8(c-d), revealed that the structure of GO@CaONPs-ES/DSAC and GO@CaONPs-FB/DSAC are still maintained even after adsorption. Furthermore, the successful interaction between MB dye and GO@CaONPs-ES/DSAC and GO@CaONPs-FB/DSAC was verified using the XPS characterization as presented. The XPS survey spectrum of GO@CaONPs-ES/DSAC+MB and GO@CaONPs-FB/DSAC+MB when compared to GO@CaONPs-ES/DSAC and GO@CaONPs-FB/DSAC revealed the presence of N 1s and S 2p core levels, which suggest that MB dye was adsorbed successfully on the surface of the adsorbent materials as revealed

in Fig. 8(e). The N 1s spectrum of GO@CaONPs-ES/DSAC+ MB presented in Fig. 8(f), were observed to be fitted with peaks at 399.5, 400.5 and 401.9 eV relating to -N=, -NH-, and -NH^{+}. The N 1s spectrum of GO@CaONPs-ES/DSAC+ MB was observed to have also been streamlined into three peaks at 398.7, 399.5 and 400.3 eV. The peaks at 398.7, 399.5 eV could be attributed to =N-R group of MB dye molecules (Qian et al., 2023). The peak at 400.3 could be assigned to -N-R. The increasing in the binding energy of GO@CaONPs-ES/DSAC+ MB (399.5, 400.5 and 401.9 eV) and of GO@CaONPs-FB/DSAC+ MB (398.7, 399.5 and 400.3 eV), indicates the existence of electrostatic interaction and hydrogen bonding. In addition, the S 2p high-resolution spectra of GO@CaONPs-ES/DSAC+ MB and GO@CaONPs-FB/DSAC+ MB displayed. in Fig. 8(g), revealed peaks at 165.5 and 164.5 relating to S $2p^{1/2}$ and S $2p^{3/2}$ respectively (Srikaew et al., 2023). The presence of S 2p and N 1s suggest that MB dye was successfully captured on GO@CaONPs-ES/DSAC and GO@CaONPs-FB/DSAC. The zeta potential measurement revealed that the PZC values of GO@CaONPs-ES/DSAC and GO@CaONPs-FB/DSAC was 3.42 and 5.04, respectively, suggesting a positively charged. Conversely, at pH > pHpzc the surfaces of GO@CaONPs-ES/DSAC and GO@CaONPs-FB/DSAC becomes negatively charged thereby promoting strong electrostatic attractive forces between the cationic MB dye molecules. The positively charged MB dye molecules (adsorbate) and the positively charged adsorbent surface were seen to repel one another (electrostatic repulsion) at pH < pHpzc.

. Furthermore, after MB dye molecules, the PZC of both adsorbents were observed to have increased to 5.91 and 6.06, suggesting that electrostatic interaction plays a major role during the uptake of MB dye on GO@CaONPs-ES/DSAC and GO@CaONPs-FB/DSAC (Liu et al., 2023). Finally, we can therefore say that MB dye interaction on the surfaces on GO@CaONPs-ES/DSAC and GO@CaONPs-FB/DSAC involved multiple mechanism such as hydrogen bonding which is established between the adsorbents functional groups (O-H, -C=O, and -COOH) and MB (–N $(CH_3)_2$), pore-filling, $\pi - \pi$ interaction between the π-electron of the MB dye aromatic benzene ring (acceptor) and π-electron of the nanocomposites (donor), and electrostatic attraction.

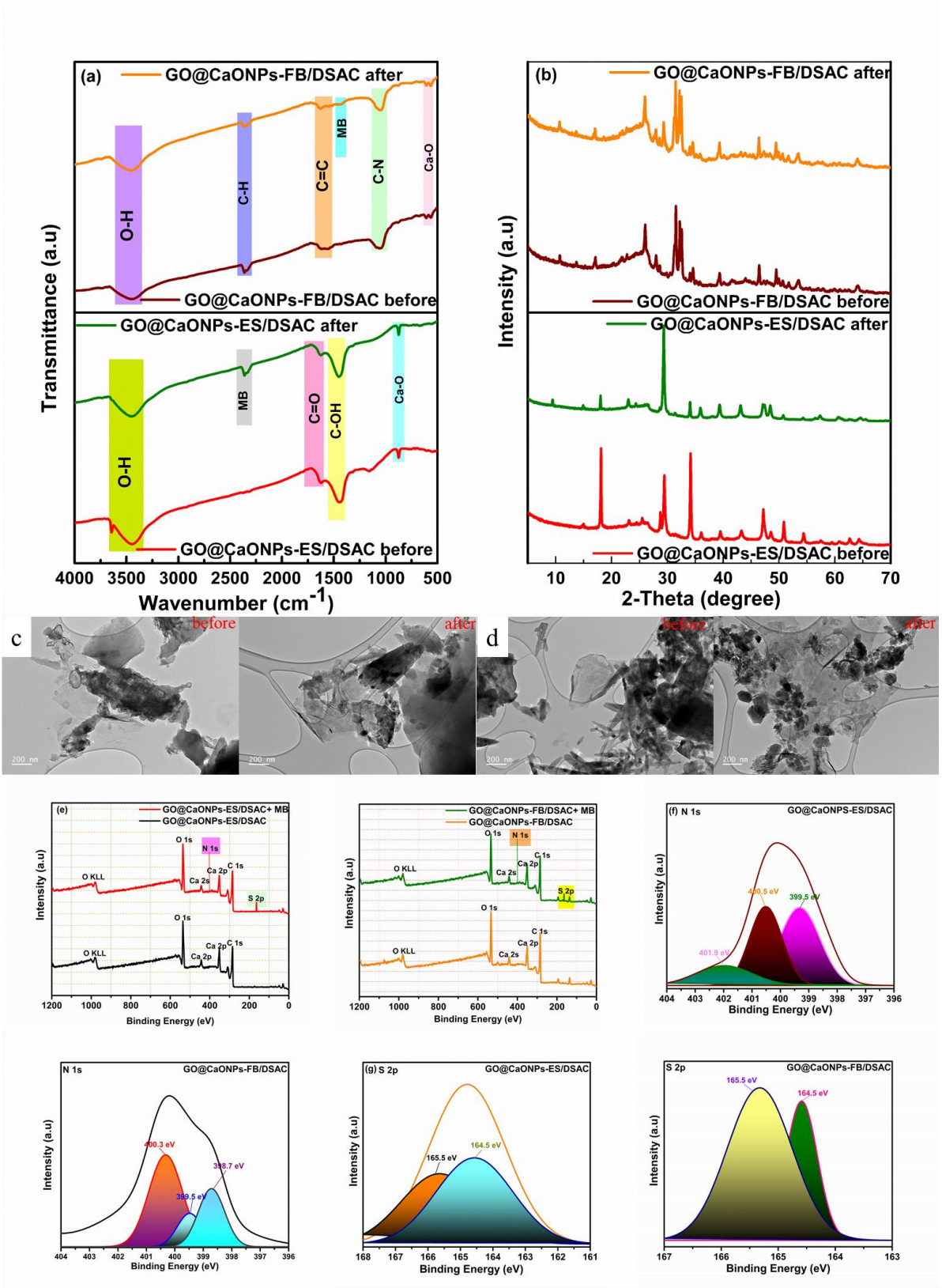

Fig. 8. (a) FT-IR, (b) XRD, TEM (c-d), and (e-g) XPS survey, N 1s, and S 2p analysis of GO@CaONPs-ES/DSAC and GO@CaONPs-FB/DSAC nanocomposites towards MB dye before and after adsorption.

The AFM analysis of GO@CaONPs-ES/DSAC and GO@CaONPs-FB/DSAC after and before MB adsorption is presented in Fig. 9(a-b). The R_a and R_q values were observed to have increased after MB adsorption. The increment can be accredited to the accumulation of MB on

the nanocomposite surfaces, suggesting that the MB was successfully adsorbed on the adsorbent surfaces without precipitation (Aziz et al., 2023).

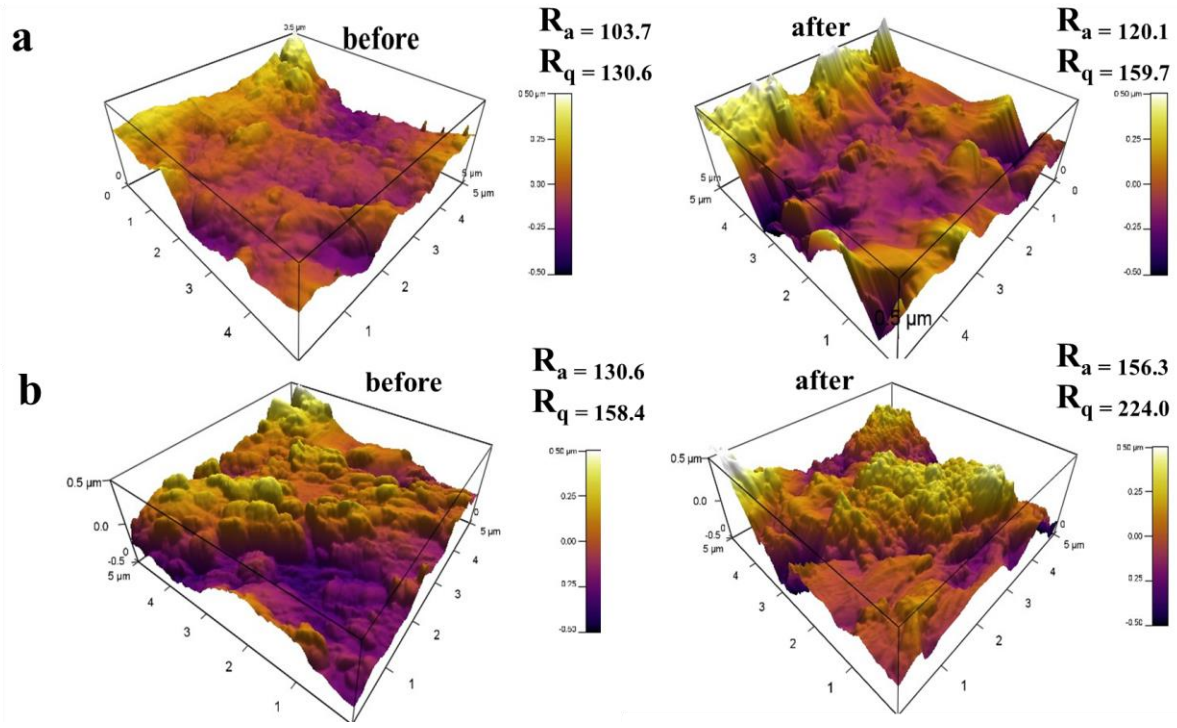

Fig. 9. AFM analysis of (a) GO@CaONPS-ES/DSAC, and (b) GO@CaONPS-FB/DSAC nanocomposite before and after MB adsorption.

3.13 Cost evaluation study

The recent use of nanocomposite as a promising and sustainable nano-adsorbents for environmental remediation has propelled the need for cost estimation to determine the material economic feasibility (GadelHak et al., 2023). Hence, cost evaluation involved in the development of GO@CaONPs-ES/DSAC, and GO@CaONPs-FB/DSAC per gram for MB dye treatment through various steps such as sample collection, electricity cost (electricity consumption during hot air oven drying, carbonization, and muffle furnace calcination), and cross-linking process were valued and presented in Table 8. The cost evaluation study showed that the total production cost of GO@CaONPs-ES/DSAC, and GO@CaONPs-FB/DSAC is approximately US$1.38/g and US$1.11/g respectively. The cost of material for the remediation of 100 m^3 (100000 L) MB dye contaminated water (50 mg/L) is only US$41.52 and US$33.30, respectivley for both adsorbents. However, the cost will reduce to US$4.15 and US$3.30 if both adsorbents are to be employed for 10 successive cycles with minimum usage and chemical cost for regeneration process. This cost evaluation study suggest that the developed adsorbent materials are sustainable, more economical and have great potential to be employed in real-time application of MB dye treatment in aqueous environment (Deb et al., 2022).

Table 8. Cost analysis of GO@CaONPs-ES/DSAC, and GO@CaONPs-FB/DSAC

	Material	Cost material description	Quantity	Cost (USD)	Total cost (USD)/ yield
1	GO	Graphite powder	5 g	0.29	
		Hydrochloric acid	10 mL	0.23	
		Sulphuric acid	100 mL	0.94	
		Hydrogen peroxide	30 mL	0.82	
		Sodium nitrate	5 g	0.13	
		Potassium permanganate	30 g	3.98	
		Electricity Cost (heating and drying)		1.76	
					8.15/ 6.68g
2	Activated carbon	Durian shell	500 g	-	
		Transportation	-	2.23	
		Potassium hydroxide	20 g	1.25	
		Hydrochloric acid	5 mL	0.12	
		Electricity cost (drying and carbonization)		2.5	
					6.10/ 43.41g
3	CaONPs-ES	Eggshell	30 g	-	
		Transportation		-	
		Sodium chloride	4 g	2.24	
		Hydrochloric acid	100 mL	2.3	
		Electricity cost (heating drying and calcination)		1.42	
					5.96/ 12.455g
4	CaONPs-FB	Fish bone	50 g	-	
		Transportation		-	
		Sodium chloride	4 g	2.24	
		Hydrochloric acid	100 mL	2.3	
		Electricity cost (heating, drying and calcination)		3.66	
					8.20/ 16.34g
5	GO@CaONPs-ES/DSAC	Maize grain	5 g	0.0012	
		DSAC	5 g	0.77	
		GO	2 g	2.44	
		CaONPs-ES	3 g	1.44	
		Electricity cost (drying, heating and calcination)		1.91	
					6.56/ 4.74 g
6	Total production cost per 1gram				1.38 / 1 g
7	Total cost of treating 50 mg/L MB in 100 m^3 (100000 litre) using 0.3 g/L				41.52/ 30 g
8	GO@CaONPs-FB/DSAC	Maize grain	5 g	0.0012	
		DSAC	5 g	0.77	
		GO	2 g	2.44	
		CaONPs-ES	3 g	1.51	

		Electricity cost (drying, heating and calcination)	1.91	
				6.63 / 5.98 g
9	Total production cost per 1 gram			1.11/ 1 g
10	Total cost of treating 50 mg/L MB in 100 m^3 (100000 litre) using 0.3 g/L			33.30/ 30 g

3.14 Design of experiment

3.14.1 Mathematical model development and analysis of variance (ANOVA)

The synergistic effects of the three parameters (temperature, adsorbent dosage and pH) on MB adsorption by GO@CaONPs-ES/DSAC and GO@CaONPs-ES/DSAC were investigated CCD. The experimental responses are recorded in Table S4. The table revealed that the highest percentage removal of MB dye by GO@CaONPs-ES/DSAC (99.90 %) and GO@CaONPs-ES/DSAC (98.97 %) was attained at run 10 (Temperature = 318, adsorbent dosage = 0.3 g/L, and pH = 8) while the lowest MB uptake was achieved at run 3 for both GO@CaONPs-ES/DSAC (47.41 %) and GO@CaONPs-ES/DSAC (44.40 %), respectively. The final empirical model coded factor with inclusion of the insignificant terms for both the MB removal by GO@CaONPs-ES/DSAC and GO@CaONPs-ES/DSAC are depicted in Equation 1-2.

$$\text{GO@CaONPs-ES/DSAC} = +94.82 + 51.16\,A - 4.68\,B + 11.48\,C + 3.26\,AB + 1.84\,AC - 2.77\,BC + 1.45\,A^2 - 10.17\,B^2 - 19.68\,C^2 \quad (15)$$

$$\text{GO@CaONPs-FB/DSAC} = +89.31 + 5.53\,A - 4.89\,B + 10.59\,C + 2.15\,AB + 0.8875\,AC - 2.88\,BC + 3.57\,A^2 - 11.85\,B^2 - 18.41\,C^2 \quad (16)$$

The ANOVA was employed to assess the model's reliability and significance. The quadratic polynomial model was selected for both responses by the ANOVA. The mean squares (MS) were calculated by dividing the sum of the squares (SS) of each variation source by the degrees of freedom (df), as shown in Table S5 (Li et al., 2021). Model terms with p-values <0.05 were considered significant, while those with p-values >0.05 were deemed insignificant. The p-values in this study were <0.0001, indicating that the model was valid and statistically significant. The F-value and P-value for the adsorption of MB on GO@CaONPs-ES/DSAC and GO@CaONPs-FB/DSAC were determined using the CCD ANOVA, resulting in values of 310.50, <0.0001 and 305.96, <0.0001, respectively. The associated P-values and calculated F-values indicated that the model was most significant and that the variation in responses could be explained by the quadratic model equation. However, the MB adsorption by GO@CaONPs-ES/DSAC model have a significant term of A, B, C, AB, AC, BC, B^2, and C^2 as significant

terms, while A^2 was insignificant. Similarly, GO@CaONPs-FB/DSAC towards MB removal significant terms are A, B, C, AB, BC, A^2, B^2, and C^2, and AC was insignificant. A high R^2 value of 0.996 for both GO@CaONPs-ES/DSAC and GO@CaONPs-FB/DSAC as presented in Table S6, suggest that the selected model predict nearly 99.6 % of the variation response. Moreover, a difference of $\leq$0.2 between adjusted R^2 and predicted R^2 for both nanocomposites towards MB removal suggests the reliability of the model (Abbasi et al., 2021). The adequate precision and coefficient of variation (CV) values 56.03 and 1.72 % and for GO@CaONPs-ES/DSAC and 58.50 and 1.33 % for GO@CaONPs-FB/DSAC, respectively. The adequate precision and CV values obtained for both composites were seen to be $\geq$4.0 and $\leq$10 %, respectively, implying that the model selected have high precision and noteworthy reproducibility (Jung et al., 2019). Furthermore, Box-Cox plots was presented in Fig. 5(a-b) to determine the models power transformation. However, a model transformation is suggested if the current lambda (λ) values lies outside of the high- and low-confidence intervals (CI) (Miyah et al., 2021). The results revealed that there is no need for model transformation because the current value ($\lambda = 1$) falls within the confidence intervals and closer to the optimum design values for GO@CaONPs-ES/DSAC (-0.09, and 1.44), and GO@CaONPs-FB/DSAC (-0.23, and 1.6). Also, the normal plot of residuals in Fig.5(c-d), showed that the experimental data points fall closely to the straight lines and that normality test P-values are greater than the threshold value (P>0.05), suggesting the analysis assumption were satisfied and that each response residual model follows a normal (Basheer, et al., 2021).

3.14.2 3-dimensional plots: effect of interactive variables

The quadratic regression models selected were utilized to develop a response surface plots, which visualized the independent and interactive contributions to the removal of MB onto GO@CaONPs-ES/DSAC and GO@CaONPs-FB/DSAC. Fig 10. displays the surface plots, where any two parameters were varied within the experimental range, while the other independent variables remained constant at their midpoints (null point). The combined effect of adsorbent dosage and temperature on MB removal onto GO@CaONPs-ES/DSAC and GO@CaONPs-FB/DSAC was shown in Fig. 10(a-b), respectively, at a constant pH of 8. The results indicated that as temperature and dosage increased simultaneously, the removal percentage increased up to a point and then slightly decreased with a further increase in dosage. The highest MB removal was observed to be 99.90% and 98.97% onto GO@CaONPs-ES/DSAC and GO@CaONPs-FB/DSAC, respectively, at 318 K and 0.3 g/L. The increase in MB removal with a temperature increase suggests an endothermic nature of the adsorption process, resulting in a build-up of kinetic energy, thereby reducing the solution viscosity and boosting the adsorptive performance of GO-based composites. The decrease in MB removal

with a further increase in dosage could be accredited to MB accumulation on the adsorbent active site as the adsorption process progresses. The plots established that the adsorption process is significantly affected by adsorbent dosage and temperature interaction. The pH and temperature interactive effect at a constant dosage of 0.3 g/L for GO@CaONPs-ES/DSAC and GO@CaONPs-FB/DSAC towards MB removal is presented in 10(c-d). It is observed from the shape of the plots that pH and temperature increase resulted in a significant MB removal increase. Based on the F-values, the solution pH has the greatest significant effect on the MB adsorption process. At high pH, the surfaces of the adsorbents become negatively charged, promoting strong electrostatic attraction between the cationic MB and the adsorbents. Furthermore, at higher temperature, there is an increase in kinetic energy and a decrease in viscosity, thereby facilitating the removal of MB dye. The interactive effect of pH and adsorbent dosage at a constant temperature of 318 K is depicted in Fig. 10(e-f). It is observed that an increase in the adsorbent dosage and pH resulted in an increase in MB removal, however, further increase resulted in a decrease in MB removal. The increase in MB removal as pH and adsorbent dosage increases could be credited to the electrostatic interaction and the presence of more adsorption sites on the adsorbent surface. The decrease in MB removal could result from the saturation of adsorbent sites with further adsorbent dosage increase. The plots revealed that the pH and adsorbent dosage pose a significant effect on the adsorption process for both adsorbents. Finally, in terms of singular interaction, it was observed that the solution pH has the greatest significant effect on MB uptake onto GO@CaONPs-ES/DSAC and GO@CaONPs-FB/DSAC, followed by temperature and adsorbent dosage. The interactive effect of temperature and adsorbent dosage was seen to have the greatest significant impact on MB adsorption on GO@CaONPs-ES/DSAC, while the interactive effect of pH and temperature gave the most significant impact on MB removal by GO@CaONPs-FB/DSAC, respectively.

3.14.3 Process optimization

The simultaneous maximization of MB removal onto GO@CaONPs-ES/DSAC and GO@CaONPs-FB/DSAC is of utmost importance because the response is related to both environmental and economic concerns. However, each independent parameter exerts a contradictory influence on the response. Therefore, numerical process optimization using the statistical software (Design Expert) was used to confirm the design suitability, alliance, and economic viability. The desirability function assign values between 0 and 1, with "0" signifying an undesired response and "1" demonstrating a desired or ideal response. The final outcome of each independent parameter was set as "within the experimental range" to evaluate the optimum conditions, while both variables response were set to "maximize" as basis. It was

revealed from the results obtained that the MB adsorption onto GO@CaONPs-ES/DSAC and GO@CaONPs-FB/DSAC nanocomposites were 99.01% and 97.12%, respectively, with an error of 0.95% and 1.31%, respectively. These values were obtained from the predicted results of 99.96% and 98.41% with a desirability of 1. The results were achieved under the optimal conditions of a temperature of 319.20 K, adsorbent dosage of 0.493 g/L, and a pH of 8.544, respectively.

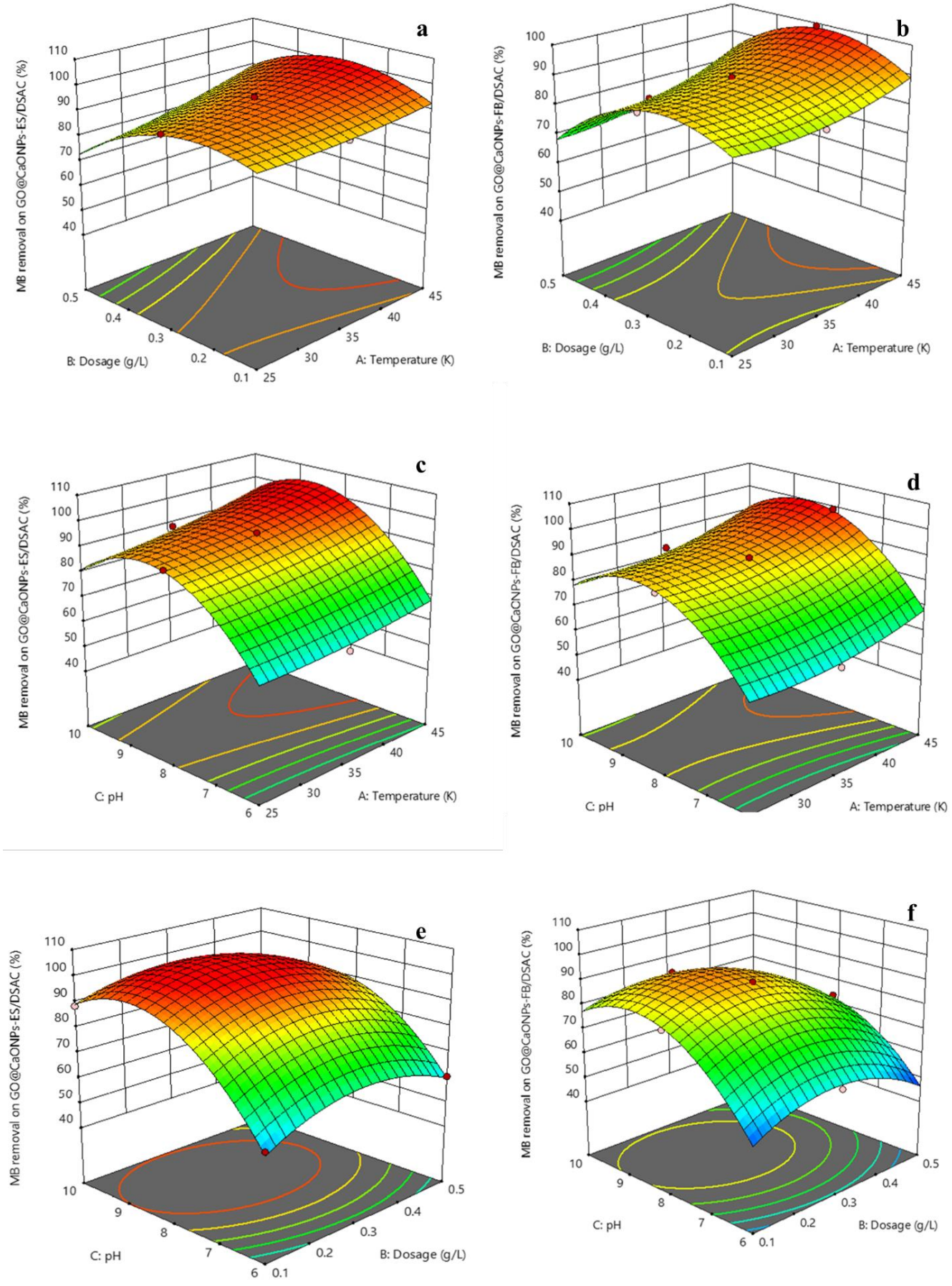
a
MB removal on GO@CaONPs-ES/DSAC (%)
B: Dosage (g/L)
A: Temperature (K)
b
MB removal on GO@CaONPs-FB/DSAC (%)
B: Dosage (g/L)
A: Temperature (K)
c
MB removal on GO@CaONPs-ES/DSAC (%)
C: pH
A: Temperature (K)
d
MB removal on GO@CaONPs-FB/DSAC (%)
C: pH
A: Temperature (K)
e
MB removal on GO@CaONPs-ES/DSAC (%)
C: pH
B: Dosage (g/L)
f
MB removal on GO@CaONPs-FB/DSAC (%)
C: pH
B: Dosage (g/L)

1167

Fig. 10. 3- dimensional surface response plots for GO@CaONPs-ES/DSAC, and GO@CaONPs-FB/DSAC towards MB removal: effect of (a-b) adsorbent dosage, and temperature (c-d) temperature, and pH and (e-f) adsorbent dosage and pH.

4. Conclusion

The need for affordable and sustainable adsorbents for waste water remediation has led to the synthesis of calcium oxide derived from eggshell and fish bone (CaONPs-ES and CaONPs-FB) incorporated on graphene oxide (GO) cross-linked with durian shell activated carbon (DSAC) using fermented maize grain extract (GO@CaONPs-ES/DSAC and GO@CaONPs-FB/DSAC). These nanocomposites were evaluated for Methylene blue (MB) dye uptake from aqueous media. The developed adsorbents exhibited well-developed porous structures with rough and uneven surfaces. The adsorption capacity of MB dye was affected by pH, adsorbent dosage, initial concentration, co-existing ions, and temperature. The negatively charged surfaces of the nanocomposites at high pH values facilitated the uptake of positively charged MB dye via electrostatic attraction. Equilibrium data for both adsorbents matched well with the Freundlich and Harkins-Jura model, suggesting heterogeneous and pore surface distribution mechanisms. The maximum adsorption capacities for GO@CaONPs-ES/DSAC and GO@CaONPs-FB/DSAC were 621.1 and 1062.8 mg/g at 298 K, respectively. The MB dye adsorption mechanism was dominated by hydrogen bonding, electrostatic interaction, π-π interaction, and physical mechanisms. The kinetics followed the pseudo-second order model, and the thermodynamic study indicated the spontaneity, endothermic nature, and orderliness of the process. The GO@CaONPs-ES/DSAC and GO@CaONPs-FB/DSAC nanocomposites demonstrated excellent adsorptive performances in real-time water applications, outperforming other reported adsorbents for MB dye removal. The reusability tests revealed that the developed adsorbents have a high-performance application for the treatment of MB dye and other pollutants from aqueous environments. The GO@CaONPs-ES/DSAC and GO@CaONPs-FB/DSAC nanocomposites offer a promising and sustainable option for the removal of MB dye and other pollutants from aqueous systems. The synergetic effect of temperature and adsorbent dosage for GO@CaONPs-ES/DSAC, and adsorbent dosage and pH for GO@CaONPs-FS/DSAC as revealed by the RSM statistical analysis was observed to have the most interaction towards MB removal with the pH having the highest singular significant effect.

Acknowledgements

The authors acknowledge the Ministry of Higher Education (MOHE), Malaysia for providing the research funding under project code FRGS/1/ 2019/TK10/CURTIN/02/2. We also thank Curtin University Malaysia for providing research facility and financial support for the project. The authors also acknowledge Curtin Malaysia Postgraduate Research Scholarship (CMPRS)

for the financial support. We also appreciate Global Centre for Environmental Remediation (GCER)'s laboratory and EMX unit, The University of Newcastle, Australia and the Surface Analysis Laboratory, MWAC, located at the University of New South Wales, Australia for instrumental support. The authors will also like to appreciate Institute of Sustainable Industries and Liveable Cities, Victoria University, Australia. The immense contribution of Dr. Arghavan Mirahsani, Environmental Engineering Manager Grafoid Inc. Innovation Park, 945 Princess Street Kingston, Ontario, Canada is also appreciated.

References

Abbasi, N., Khan, S. A., Khan, T. A., 2021. Response surface methodology mediated process optimization of Celestine blue B uptake by novel custard apple seeds activated carbon/ $FeMoO_4$ nanocomposite, Journal of Water Process Engineering, 43, 102267.

Abdoul, H., Yi, M., Prieto, M., Yue, H., Ellis, G. J., Clark, J. H., Budarin, V. L., Shuttleworth, P. S., 2023. Efficient adsorption of bulky reactive dyes from water using sustainably-derived mesoporous carbons, Environmental Research, 221, 115254.

Abutaleb, A., Imran, M., Zouli, N., Khan, A. H., Hussain, S., Ali, M. A., Bakather, O., Gondal, M. A., Khan, N. A., Panchal, H., Zahmatkesh, S., 2023. Fe_3O_4-multiwalled carbon nanotubes-bentonite as adsorbent for removal of methylene blue from aqueous solutions, Chemosphere, 137824.

Abutaleb, A., Imran, M., Zouli, N., Khan, A. H., Hussain, S., Ali, M. A., Bakather, O., Gondal, M. A., Khan, N. A., Panchal, H., Zahmatkesh, S., 2023. Fe3O4-multiwalled carbon nanotubes-bentonite as adsorbent for removal of methylene blue from aqueous solutions, Chemosphere 316, 137824.

Adedeji, O. M., Jahan, K., 2023. Removal of pollutants from aqueous product of Co-hydrothermal liquefaction: Adsorption and isotherm studies, Chemosphere, 321, 138165.

Ahmadijokani, F., Molavi, H., Bahi, A., Wuttke, S., Kamkar, M., Rojas, O. J., Ko, F., Arjmand, M., 2023. Electrospun nanofibers of chitosan/polyvinyl alcohol/UiO-66/nanodiamond: Versatile adsorbents for wastewater remediation and organic dye removal, Chemical Engineering Journal, 475, 141176.

Ahsani-Namin, Z., Norouzbeigi, R., Shayesteh, H., 2022. Green mediated combustion synthesis of copper zinc oxide using *Eryngium planum* leaf extract as a natural green fuel: Excellent adsorption capacity towards Congo red dye, Ceramics International, 48(14), 20961-20973.

Alsohaimi, I. H., Alhumaimess, M. S., Alqadami, A. A., Alshammari, G. T., Al-Olaimi, R. F., Abdeltawab, A. A., El-Sayed, M. Y., Hassan, H. M., 2023. Adsorptive performance of aminonaphthalenesulfonic acid modified magnetic-graphene oxide for methylene blue dye: Mechanism, isotherm and thermodynamic studies Inorganic Chemistry Communications, 147, 110261.

Aziz, T., Farid, A., Chinnam, S., Haq, F., Kiran, M., Wani, A.W., Alothman, Z. A., Aljuwayid, A. M., Habila, M. A., Akhtar, M. A.,2023. Synthesis, characterization and adsorption behavior of modified cellulose nanocrystals towards different cationic dyes, Chemosphere, 321,137999.

Basheer, A. O., Hanafiah, M. M., Alsaadi, M. A., Al-Douri, Y., Al-Raad, A. A., 2021. Synthesis and optimization of high surface area mesoporous date palm fiber-based nanostructured powder activated carbon for aluminum removal, Chinese Journal of Chemical Engineering, 32, 472–484

Bezerra de Araujo, C. M., Wernke, G., Ghislandi, M. G., Diório, A., Vieira, M. F., Bergamasco, R., Sobrinho, M. A. M., Rodrigues, A. E., 2023. Continuous removal of pharmaceutical drug chloroquine and Safranin-O dye from water using agar-graphene oxide hydrogel: Selective adsorption in batch and fixed-bed experiments, Environmental Research, 216, 114425.

Biswal, H. J., Yadav, A., Vundavilli, P. R., Gupta, A., 2021. High aspect ZnO nanorod growth over electrodeposited tubes for photocatalytic degradation of EtBr dye, RSC Advances, 11,1623-1634.

Bozacı, G., Acaralı, N., 2023. Chemical production of activated carbon from green coffee with adsorption isotherm support by Taguchi model, Journal of the Indian Chemical Society, 100(1), 100864.

Chen, Z., Pan, Y., Cai, P., 2022. Sugarcane cellulose-based composite hydrogel enhanced by g-C_3N_4 nanosheet for selective removal of organic dyes from water, International Journal Biological Macromolecules, 205, 37-48.

Chouaybi, I., Ouassif, H., Bettach, M., Moujahid, E, M., 2022. Fast and high removal of acid red 97 dye from aqueous solution by adsorption onto a synthetic hydrocalumite: Structural characterization and retention mechanisms, Inorganic Chemistry Communications, 146, 110169.

Dahlan, I., Keat, O. H., Aziz, H. A., Hung, Y. T., 2023. Synthesis and characterization of MOF-5 incorporated waste-derived siliceous materials for the removal of malachite green dye from aqueous solution, Sustainable Chemistry and Pharmacy, 31, 100954.

Dan, S., Bagheri, H., Shahidizadeh, A., Hashemipour, H., 2023. Performance of graphene Oxide/SiO_2 Nanocomposite-based: Antibacterial Activity, dye and heavy metal removal, Arabian Journal of Chemistry, 16(2), 104450.

Deb, A. K., Biswas, B., Rahman, M. M., Xi, Y., Paul, S. K., Naidu**,** R., 2023. Magnetite Nanoparticles Loaded into Halloysite Nanotubes for Arsenic(V) Removal from Water, *ACS* Applied Nano Materials, 5(9), 12063–12076.

Debnath, S., Das, R., 2023. Strong adsorption of CV dye by Ni ferrite nanoparticles for waste water purification: Fits well the pseudo second order kinetic and Freundlich isotherm model, Ceramics International,

Dedecan, T., Baylan, N., Inci, I., 2022. Synthesis, characterization and application of calcium peroxide nanoparticles as a novel adsorbent for removal of malic acid from aqueous solutions Chemical Physics Letters, 797, 139581.

Dolas, H., 2023. Activated carbon synthesis and methylene blue adsorption from pepper stem using microwave assisted impregnation method: Isotherm and kinetics, Journal of King Saud University - Science, 102559.

Du, P., Zhang, J., Cai, Z., Ge, F., 2023. High adsorption of cationic dyes from aqueous solution using worm-like porous nanosilica: Isotherm, kinetics and thermodynamics, Materialstoday Communications, 35, 05697.

El-Ghobashy, M. A., Salem, I. A., El-Dahrawy, W. M., Salem, M. A., 2023. Fabrication of α-MnO_2/Fe-Mn binary oxide nanocomposite as an efficient adsorbent for the removal of methylene blue from wastewater, Journal of Molecular Structure, 1272, 134118.

Gaayda, J. E., Titchou, F. E., Oukhrib, R., Karmal, I., Oualid, H. A., Berisha, A., Zazou, H., Swanson, C., Hamdani, M., Akbour, R. A., 2022. Removal of cationic dye from coloured water by adsorption onto hematite-humic acid composite: Experimental and theoretical studies, Separation and Purification Technology, 288, 120607.

GadelHak, Y., El-Azazy, M., Shibl, M. F., Mahmoud, R. K., 2023. Cost estimation of synthesis and utilization of nano-adsorbents on the laboratory and industrial scales: A detailed review, Science of The Total Environment, 162629.

Gajera, R., Patel, R. V., Yadav, A., Labhasetwar, P. K., 2022. Adsorption of cationic and anionic dyes on photocatalytic flyash/TiO_2 modified chitosan biopolymer composite, Journal of Water Process Engineering, 49, 102993.

George, S. C., Rajan, R., Aprem, A. S., Thomas, S., Kim, S. S., 2016. The fabrication and properties of natural rubber-clay nanocomposites, Polymer Testing, 51,165-173.

Ghaffari, A. D., Barati, M., Saryazdi, A. K. P., Ghaffarifar, F., Pirestani, M., Ebrahimi. M., 2023. In vitro and in vivo study on antiprotozoal activity of calcium oxide (CaO) and magnesium oxide (MgO) nanoparticles on promastigote and amastigote forms of Leishmania major, Acta Tropica, 238, 106788.

Guo, T., Bulin, C., 2021. Facile fabrication of MgO/graphene oxide composite as an efficient adsorbent for rapid removal of aqueous organic dyes: Performance evaluation and mechanistic investigation, Journal of Physics and Chemistry of Solids, 158, 110251.

Gurav, R., Bhatia, S. K., Choi, T. R., Kim, H. J., Choi, Y-K., Lee, H-J., Ham, S., Cho, J. Y., Kim, S. H., Lee, S. H., Yun, J., Yang, Y-H., 2023. Adsorptive removal of synthetic plastic components bisphenol-A and solvent black-3 dye from single and binary solutions using pristine pinecone biochar, Chemosphere, 296, 134034.

Hadadi, A., Imessaoudene, A., Bollinger, J. C., Bouzaza, A., Amrane, A., Tahraoui, H., Mouni, J., 2023. Aleppo pine seeds (*Pinus halepensis* Mill.) as a promising novel green coagulant for the removal of Congo red dye: Optimization via machine learning algorithm, Journal of Environmental Management, 331, 117286.

Han, X., Zhao, Y., Zhao, F., Wang, F., Tian, G., Liang, J., 2023. Novel synthesis of nanoscale zero-valent iron from iron ore tailings and green tea for the removal of methylene blue, Colloids and Surfaces A: Physicochemical and Engineering Aspects, 656, 130412.

He, Y. Z., Peng, L., Xiong, H., Liu, W., Zhang, H., Peng, X., Zhu, X., Guo, F., Sun, Y., 2022. The profiles of durian (*Durio zibethinus Murr*.) shell phenolics and their antioxidant effects on H_2O_2-treated HepG2 cells as well as the metabolites and organ distribution in rats, Food Research International, 163, 112122.

Jawad, A. H., Abdulhameed, A. S., Surip, S. N., Alothman, Z. A., 2023. Hybrid multifunctional biocomposite of chitosan grafted benzaldehyde/montmorillonite/algae for effective removal of brilliant green and reactive blue 19 dyes: Optimization and adsorption mechanism, Journal of Cleaner Production, 393, 136334.

Joshiba, G. J., Kumar, P. S., Rangasamy, G., Ngueagni, P. T., Pooja, G., Balji, G. B., Alagumalai, K., El-Serehy, H. A., 2022. Iron doped activated carbon for effective removal of tartrazine and methylene blue dye from the aquatic systems: Kinetics, isotherms, thermodynamics and desorption studies, Environmental Research, 215(3), 114317.

Jung, K-W., Choi, B. H., Song, K. G., Choi, J. W., 2019. Statistical optimization of preparing marine macroalgae derived activated carbon/iron oxide magnetic composites for sequestering acetylsalicylic acid from aqueous media using response surface methodologys, Chemosphere 215, 432-443.

Kasirajan, R., Bekele, A., Girma, E., 2022. Adsorption of lead (Pb-II) using CaO-NPs synthesized by sol gel process from hen eggshell: Response surface methodology for modeling, optimization and kinetic studies, South African Journal of Chemical Engineering, 40, 209-229.

Kaveh, R., Bagherzadeh, M., 2022. Simultaneous removal of mercury ions and cationic and anionic dyes from aqueous solution using epichlorohydrin cross-linked chitosan @ magnetic Fe_3O_4/activated carbon nanocomposite as an adsorbent, Diamond and Related Materials, 124, 108923.

Kayanja, O., Hassan, M. A., Hassanin, A., Ohashi, H., Khalil, A. S. G., 2023. Effect of phase disparity of MoS_2 nanosheets on the performance of PES membranes for dual industrial oil-in-water emulsion separation and dyes adsorption, Process Safety and Environmental Protection, 171, 55-70.

Khiam, G. K., Karri, R. R., Mubarak, N. M., Khalid, M., Walvekar, R., Abdullah, E. C., Rahman, M. E., 2022. Modelling and optimization for methylene blue adsorption using graphene oxide/chitosan composites via artificial neural network-particle swarm optimization, Materialstoday Chemistry, 24, 100946.

Khnifira, M., Boumya, W., Attarki, J., Mahsoune, A., Abdennouri, M., Sadiq, M., Kaya, S., Barka, N., 2023. Adsorption characteristics of dopamine by activated carbon: Experimental and theoretical approach, Journal of Molecular Structure, 1278, 134964.

Kim, S-H., Kim, D-S., Moradi, H., Chang, Y-Y., Yang, J-K., 2023. Highly porous biobased graphene-like carbon adsorbent for dye removal: Preparation, adsorption mechanisms and optimization, Journal of Environmental Chemical Engineering, 11(2), 109278.

Kojo, A. E., Cho, W., Park, C., 2022. Mildly oxidized porous covalent triazine frameworks with rapid and high adsorption capability for aqueous organic micropollutants, Journal of Industrial and Engineering Chemistry 116, 250–256.

Kumari, N., Behera, M., Singh, R., 2023. Facile synthesis of biopolymer decorated magnetic coreshells for enhanced removal of xenobiotic azo dyes through experimental modelling, Food and Chemical Toxicology, 171, 113518.

Li, W., Wei, H., Liu, Y., Li, S., Wang, G., Han, H., 2021. Fabrication of novel starch-based composite hydrogel microspheres combining Diels-Alder reaction with spray drying for MB adsorption, Journal of Environmental Chemical Engineering, 9, 105929.

Lin, G., Zeng, B., Liu, X., Li, J., Zhang, B., Zhang, L., 2022. Enhanced performance of functionalized MOF adsorbents for efficient removal of anthropogenic Hg(II) from water, Journal of Cleaner Production, 381, 134766.

Liu, A., He, S., Zhang, J., Liu, J., Shao, W., 2023. Preparation and characterization of novel cellulose based adsorbent with ultra-high methylene blue adsorption performance, Materials Chemistry and Physics, 296,127261

Lotfy, D., El-Sayyad, G. S., Shehata, N., 2023. Hexamethylenetetramine functionalized graphene oxide-alginate beads nanocomposite as efficient sorbent for dye from aqueous solution, International Journal of Biological Macromolecules, 228, 754-772.

Luo, M., Wang, L., Li, H., Bu, Y., Zhao, Y., Cai, J., 2023. Hierarchical porous biochar from kelp: Insight into self-template effect and highly efficient removal of methylene blue from water, Bioresource Technology, 372,128676

Mechnou, I., Meskini, S., El Ayar, D., Lebrun, L., Hlaibi, M., 2022. Olive mill wastewater from a liquid biological waste to a carbon/oxocalcium composite for selective and efficient removal of methylene blue and paracetamol from aqueous solution, Bioresource Technology, 365, 128162.

Mirzaei, K., Mohammadi, A., Jafarpour, E., Shojaei, A., Moghaddam, A. L., 2022. Improved adsorption performance of ZIF-8 towards methylene blue dye by hybridization with nanodiamonds, Journal of Water Process Engineering, 50, 103254.

Miyah, Y., Benjelloun, M., Lahrichi, A., Mejbar, F., Iaich, S., El Mouhri, G., Kachkoul, R., Zerrouq, F., 2021. Highly-efficient treated oil shale ash adsorbent for toxic dyes removal: Kinetics, isotherms, regeneration, cost analysis and optimization by experimental design, Journal of Environmental Chemical Engineering, 9, 106694.

Mohammad-Rezaei, M., Khalilzadeh, B., Rahimi, F., Rezaee, P., Arab, S, S., Derakhshankhah, H., Jaymand, M., 2022. Simultaneous removal of cationic dyes from simulated industrial wastewater using sulfated alginate microparticles, Journal of Molecular Liquids, 363, 119880.

Moradi, O., Pudineh, A., Sedaghat, S., 2022. Synthesis and characterization Agar/GO/ZnO NPs nanocomposite for removal of methylene blue and methyl orange as azo dyes from food industrial effluents, Food and Chemical Toxicology, 169, 113412.

Narayanam, P. K., Vishwakarma, R. K., Polaki, S. R., 2022. Fabrication of free standing graphene oxide membranes for efficient adsorptive removal of cationic dyes, Journal of Molecular Liquids, 368, 120787.

Nazir, M. M., Noman, M., Ahmed, T., Ali, S., Ulhassan, Z., Zeng, F., Zhang, G., 2022. Exogenous calcium oxide nanoparticles alleviate cadmium toxicity by reducing Cd uptake and enhancing antioxidative capacity in barley seedlings, Journal of Hazardous Materials, 438, 129498.

Ndagijimana, P., Liu, X., Xu, Q., Li, Z., Pan, B., Wang, Y., 2022. Simultaneous removal of ibuprofen and bisphenol A from aqueous solution by an enhanced cross-linked activated carbon and reduced graphene oxide composite, Separation and Purification Technology, 299, 121681.

Ndagijimana, P., Liu, X., Xu, Q., Lai, D., Wang, G., Pan, B., Wang, Y., 2021. Cassava flour extracts solution to induce gelatin cross-linked activated carbon-graphene oxide composites: The adsorption performance of dyes from aqueous media, Environmental Advances, 5, 100079.

Neolaka, Y. A. B., Riwu, A. P. P., Aigbe, U. O., Ukhurebor, K. U., Onyancha, R. B., Darmokoesoemo, H., Kusuma, H. S., 2023. Potential of activated carbon from various sources as a low-cost adsorbent to remove heavy metals and synthetic dyes, Results in Chemistry, 5, 100711.

Nizam, N. U. M., Hanafiah, M. M., Mahmoudi, E., Mohammad, A. W., Oyekanmi, A. A., 2022. Effective adsorptive removal of dyes and heavy metal using graphene oxide based Pre-treated with NaOH / H_2SO_4 rubber seed shells synthetic graphite Precursor: Equilibrium Isotherm, kinetics and thermodynamic studies, 289, 120730.

Obayomi, K. S., Lau, S. Y., Danquah, M. K. Chiong, T., Takeo, M., 2022. Advances in graphene oxide based nanobiocatalytic technology for wastewater treatment, Environmental Nanotechnology, Monitoring & Management 17, 100647.

Obayomi, K. S., Lau, S. Y., Zahir, A., Meunier, L., Zhang, J., Dada, A. O., Rahman, M. M., 2023a. Removing methylene blue from water: A study of sorption effectiveness onto nanoparticles-doped activated carbon, Chemosphere, 313, 137533.

Obayomi, K. S., Lau, S. Y., Mayowa, I. E., Danquah, M. K., Jianhua, Z., Chiong, T., Meunier, L., Rahman, M. M., 2023b. Recent advances in graphene-derived materials for biomedical waste treatment, Journal of Water Process Engineering 51, 103440.

Obayomi, K. S., Lau, S. Y., Ibrahim, O., Jianhua, Z., Meunier, L., Maduakolam, A. M., Taiwo, A. B., Pramanik, B. K., Rahman, M. M., 2023c. Removal of Congo red dye from aqueous environment by zinc terephthalate metal organic framework decorated on silver nanoparticles-loaded biochar: mechanistic insights of adsorption, Microporous and Mesoporous Materials

Prajapati, A. K., Mondal, M. K., 2020. Comprehensive kinetic and mass transfer modeling for methylene blue dye adsorption onto CuO nanoparticles loaded on nanoporous activated carbon prepared from waste coconut shell, Journal of Molecular Liquids, 307, 112949.

Qian, S., Changlong, W., Lixin, Z., Yanzhao, Y., 2022. Thiourea crosslinked-amino modified graphene nanoflakes as an effective adsorbent to confine Cr(VI) via multiple combination mechanisms, Journal of Cleaner Production 374, 134030.

Rajendiran, R., Patchaiyappan, A., Harisingh, S., Balla, P., Paari, A., Ponnala, B., Perupogu, V., Lassi, U., Seelam. P. K., 2022. Synergistic effects of graphene oxide grafted chitosan & decorated MnO_2 nanorods composite materials application in efficient removal of toxic industrial dyes, Journal of Water Process Engineering, 47, 102704.

Raza, A., Shoeb, M., Mashkoor, F., Rahaman, S., Mobin, M., Jeong, C., Ansari, M.Y., Ahmad, A., Phoenix dactylifera mediated green synthesis of Mn doped ZnO nanoparticles and its adsorption performance for methyl orange dye removal: A comparative study, Materials Chemistry and Physics, 286, 126173.

Rostamian, M., Hosseini, H., Fakhri, V., Talouki, P. Y., Farahani, M., Gharehtzpeh, A. J., Goodarzi, V., Su, C. H., 2022. Introducing a bio sorbent for removal of methylene blue dye based on flexible poly(glycerol sebacate)/chitosan/graphene oxide ecofriendly nanocomposites, Chemosphere, 289, 133219.

Saeed, T., Naeem, A., Din, I. U., Farooq, M., Khan, I. W., Hamayun, M., Malik, T., 2022. Synthesis of chitosan composite of metal-organic framework for the adsorption of dyes; kinetic and thermodynamic approach, Journal of Hazardous Materials, 427, 127902.

Said, H. A., Bourhim, I. A., Ouarga, A., Iraola-Arregui, I., Lahcini, M., Barroug, A., Noukrati, H., Youcef, H. B., 2023. Sustainable phosphorylated microcrystalline cellulose toward enhanced removal performance of methylene blue International Journal of Biological Macromolecules, 225, 1107-1118.

Sarkar, R., Das, D., Chanda, K., Das, B., Sarkar, S., Chattopadhyay, K. K., 2022. Hydrothermal synthesis of GO wrapped BiOCl nanosheet and its application in visible light assisted catalytic degradation of Rhodamine B dye, Materials Chemistry and Physics, 279, 125796.

Sellaoui, L., Bouzidi, M., Franco, D. S. P., Alshammari, A. S., Gandouzi, M., Georgin, J., Mohamed, N. B. H., Erto, A., Badawi, M., 2023. Exploitation of Bauhinia forficata residual fruit powder for the adsorption of cationic dyes, Chemical Engineering Journal, 456, 141033.

Shaikh, W. A., Kumar, A., Chakraborty, S., Naushad, M., Islam, R. U., Bhattacharya, T., Datta, S., 2022. Removal of toxic dye from dye-laden wastewater using a new nanocomposite material: Isotherm, kinetics and adsorption mechanism, 308, 136413.

Shi, Y., Chang, Q., Zhang, T., Song, G., Sun, Y., Ding, G., 2022. A review on selective dye adsorption by different mechanisms, Journal of Environmental Chemical Engineering, 10(6), 108639.

Singh, S., Naik, T. S. S. K., Anil, A. G., Khasnabis, S., Nath, B., Basavaraju, U, Kumar, V., Garg, V. K., Subramanian, S., Singh, J., Ramamurthy, P. C., 2022. A novel CaO nanocomposite cross linked graphene oxide for Cr(VI) removal and sensing from wastewater, Chemosphere, 301, 134714.

Srikaew, M., Jumpapaeng, P., Suwanakood, P., Kaiyasuan, C., Promarak, V., Saengsuwan, S., 2023. Rapid synthesis and optimization of UV-photopolymerized cassava starch-based superabsorbent hydrogels as a biodegradable, low-cost, and effective adsorbent for MB removal, Journal of Industrial and Engineering Chemistry, 118, 53-69.

Tamer, Y., Koşucu, A., Berber, H., 2022. Graphene oxide incorporated chitosan/acrylamide/itaconic acid semi-interpenetrating network hydrogel bio-adsorbents for highly efficient and selective removal of cationic dyes, International Journal of Biological Macromolecules, 219, 273-289.

Thanh, N. C., Shanmugam, S., Shanmugasundaram, S., AlSalhi, M. S., Devanesan, S., Shanmuganathan, R., Chi, N. T. L., 2022. Comparison of *Simarouba glauca* seed shell carbons for enhanced direct red 12B dye adsorption: Adsorption isotherm and kinetic studies Food and Chemical Toxicology, 168, 113326.

Thanh, N. C., Shanmugam, S., Shanmugasundaram, S., AlSalhi, M. S., Devanesan, S., Shanmuganathan, R., Chi, N. T. L., 2022. Comparison of *Simarouba glauca* seed shell carbons for enhanced direct red 12B dye adsorption: Adsorption isotherm and kinetic studies, Food and Chemical Toxicology, 168, 113326.

Tran, M. L., Tran, T. T. V., Juang, R. S., Nguyen, C. H., 2023. Graphene oxide crosslinked chitosan composites for enhanced adsorption of cationic dye from aqueous solutions, Journal of the Taiwan Institute of Chemical Engineers, 142, 104678

Wang, X. X., Liu, L., Li, Q-F., Xiao, H., Wang, M. L., Tu, H-C., Lin, J. M., Zhao, R-S., 2023. Nitrogen-rich based conjugated microporous polymers for highly efficient adsorption and removal of COVID-19 antiviral drug chloroquine phosphate from environmental waters, Separation and Purification Technology, 305,122517.

Wu, Y., Zhong, J., Liu, B., 2023. Effective removal of methylene blue with zero-valent iron/tea residual biochar composite: Performance and mechanism, Bioresource Technology, 371,128592.

Yang, F., Jiang, Y., Dai, M., Hou, X., Peng, C., 2022. Active biochar-supported iron oxides for Cr(VI) removal from groundwater: Kinetics, stability and the key role of FeO in electron-transfer mechanism, Journal of Hazardous Materials, 424, 127542

Yu, Dong, H., Zheng, Y., Liu, W., 2021. Ternary metal oxide embedded carbon derived from metal organic frameworks for adsorption of methylene blue and acid red 73, Chemosphere 280, 130567.

Yu, S., Pang, H., Huang, S., Tang, H., Wang, S., Qiu, M., Chen, Z., Yang, H., Song, G., Fu, D., Hu, B., Wang, X., 2021. Recent advances in metal-organic framework membranes for water treatment: A review, Science of the Total Environment, 800,149662.

Zhang, C., Dai, Y., Wu, Y., Lu, G., Cao, Z., Cheng, J., Wang, K., Yang, H., Xia, Y., Wen, X., 2022. Facile preparation of polyacrylamide/chitosan/Fe3O4 composite hydrogels for effective removal of methylene blue from aqueous solution, Carbohydrate Polymer, 234, 115882.

Zhang, S., Fan. X., Xue, J., 2023. A novel magnetic manganese oxide halloysite composite by one-pot synthesis for the removal of methylene blue from aqueous solution, Journal of Alloys and Compounds, 930, 167050.

Zhang, T., Li, M., Chen, L., Bai, H., Wang, W., Zhao, Y., 2023b. Novel montmorillonite nanosheets-based hydrogel beads with high adsorption performance and structural strength for removal of dyes and heavy metals, Chemical Physics Letters, 813,140322.

Zhu, H., Chen, S., Duan, H., He, J., Luo, Y., 2023a. Removal of anionic and cationic dyes using porous chitosan/carboxymethyl cellulose-PEG hydrogels: Optimization, adsorption kinetics, isotherm and thermodynamics studies, International Journal of Biological Macromolecules, 123213.

Zhu, H., Zhu, E., Xie, Y., Liu, D., Hu, Y., Shi, Z., Xiong, C., Yang, Q., 2022. Hydrangea-like nanocellulose microspheres with high dye adsorption and drug encapsulation prepared by emulsion method, Carbohydrate Polymers, 296,119947.

Zhu, H., Chen, S., Duan, H., He, J., Luo, Y., 2023. Removal of anionic and cationic dyes using porous chitosan/carboxymethyl cellulose-PEG hydrogels: Optimization, adsorption kinetics, isotherm and thermodynamics studies, International Journal of Biological Macromolecules, 231, 123213.

Zong, P., Wang, S., Liang, G., Shao, M., Yan, N., Xu, X., Xu, M., Li, W., Yang, Y., Chen, J., Qiu, Z., 2022. Eco-friendly approach for effective removal for Congo red dye from wastewater using reusable Zn-Al layered double hydroxide anchored on multiwalled carbon nanotubes supported sodium dodecyl sulfonate composites, Journal of Molecular Liquids 349, 118468.

1542